JEM Journal of Experimental Medicine

ARTICLE

SOAT1 promotes mevalonate pathway dependency in pancreatic cancer

Tobiloba E. Oni[1,2,3*], Giulia Biffi[1,2,4*], Lindsey A. Baker[1,2**], Yuan Hao[1**], Claudia Tonelli[1,2], Tim D.D. Somerville[1], Astrid Deschênes[1,2], Pascal Belleau[1], Chang-il Hwang[1,2,5], Francisco J. Sánchez-Rivera[6], Hilary Cox[1], Erin Brosnan[1,2], Abhishek Doshi[1,2], Rebecca P. Lumia[1,2], Kimia Khaledi[1,2], Youngkyu Park[1,2], Lloyd C. Trotman[1], Scott W. Lowe[6,7], Alexander Krasnitz[1], Christopher R. Vakoc[1], and David A. Tuveson[1,2]

Pancreatic ductal adenocarcinoma (PDAC) has a dismal prognosis, and new therapies are needed. Altered metabolism is a cancer vulnerability, and several metabolic pathways have been shown to promote PDAC. However, the changes in cholesterol metabolism and their role during PDAC progression remain largely unknown. Here we used organoid and mouse models to determine the drivers of altered cholesterol metabolism in PDAC and the consequences of its disruption on tumor progression. We identified sterol *O*-acyltransferase 1 (SOAT1) as a key player in sustaining the mevalonate pathway by converting cholesterol to inert cholesterol esters, thereby preventing the negative feedback elicited by unesterified cholesterol. Genetic targeting of *Soat1* impairs cell proliferation in vitro and tumor progression in vivo and reveals a mevalonate pathway dependency in p53 mutant PDAC cells that have undergone p53 loss of heterozygosity (LOH). In contrast, pancreatic organoids lacking p53 mutation and p53 LOH are insensitive to SOAT1 loss, indicating a potential therapeutic window for inhibiting SOAT1 in PDAC.

Introduction

Pancreatic ductal adenocarcinoma (PDAC) is a lethal malignancy with a 5-yr survival rate of <10% (Siegel et al., 2019). This poor prognosis is mostly due to late diagnosis and lack of effective therapies. Although activating KRAS mutations and inactivating p53 mutations are well-established genetic drivers of PDAC, efforts to directly target them have not led to effective treatments for the majority of PDAC patients (Hallin et al., 2020). Consequently, the focus has shifted to targeting oncogenic programs downstream of KRAS and p53, including metabolic pathways (Halbrook and Lyssiotis, 2017; Humpton et al., 2019; Sousa et al., 2016; Ying et al., 2012). In particular, emerging studies suggest that altered cholesterol metabolism is a vulnerability for cancer cells (Riscal et al., 2019).

Cholesterol is an essential component of the cell membrane, and thus it is a requirement for rapidly proliferating tumor cells. Cholesterol can be either acquired extracellularly through receptor-mediated endocytosis of low-density lipoproteins (LDL) or synthesized de novo from acetyl coenzyme A through the mevalonate pathway (Ikonen, 2008). The mevalonate pathway and cholesterol uptake are regulated by the transcription factor sterol-regulatory-element-binding protein 2 (SREBP2). SREBP2 is synthesized as an inactive, membrane-bound precursor in the ER. When intracellular cholesterol levels are low, SREBP2 translocates to the Golgi apparatus, where it undergoes proteolytic cleavage to its mature, active form (Brown and Goldstein, 1997; Horton et al., 2002). Mature SREBP2 undergoes nuclear translocation and induces the expression of several mevalonate pathway and cholesterol uptake genes, including LDL receptor (*LDLR*) and 3-hydroxy-3-methylglutaryl-coenzyme A reductase (*HMGCR*; Radhakrishnan et al., 2008). HMGCR is the rate-limiting enzyme of the mevalonate pathway and the target of statins, a class of cholesterol-lowering drugs (Endo, 1992; Larsson, 1996). SREBP2-mediated de novo cholesterol synthesis requires substantial NADPH and ATP (Coates and Brown, 2019). Moreover, the accumulation of excess cholesterol can disrupt cellular function (Fu et al., 2012; Maxfield and Tabas, 2005). For these reasons, cholesterol biosynthesis is subject to feedback inhibition by intracellular cholesterol, which tightly regulates the mevalonate pathway. Particularly, cholesterol promotes the degradation of HMGCR

[1]Cold Spring Harbor Laboratory, Cold Spring Harbor, NY; [2]Lustgarten Foundation Pancreatic Cancer Research Laboratory, Cold Spring Harbor, NY; [3]Graduate Program in Molecular and Cellular Biology, Stony Brook University, Stony Brook, NY; [4]Cancer Research UK Cambridge Institute, University of Cambridge, Cambridge, UK; [5]Department of Microbiology and Molecular Genetics, University of California, Davis, Davis, CA; [6]Department of Cancer Biology and Genetics, Memorial Sloan-Kettering Cancer Center, New York, NY; [7]Howard Hughes Medical Institute, Memorial Sloan-Kettering Cancer Center, New York, NY.

*T.E. Oni and G. Biffi contributed equally to this paper; **L.A. Baker and Y. Hao contributed equally to this paper; Correspondence to David A. Tuveson: dtuveson@cshl.edu.

and also prevents the Golgi translocation and consequential proteolytic maturation of SREBP2 (Radhakrishnan et al., 2008). Excess cholesterol can be converted into inert cholesterol esters by ER membrane-bound sterol-*O* acyltransferase 1 (SOAT1, also known as ACAT1), which is ubiquitously expressed, and SOAT2 (also known as ACAT2), whose expression is restricted to hepatic and gastrointestinal tissues (Anderson et al., 1998; Cases et al., 1998; Oelkers et al., 1998). Cholesterol esters are stored in cytosolic lipid droplets, from which cholesterol can reenter the intracellular pool by the action of neutral cholesterol ester hydrolase (Ghosh et al., 2003). Additionally, excess intracellular cholesterol can be secreted through ATP-binding cassette transporters, such as ABCA1 (Hozoji-Inada et al., 2011; Oram and Vaughan, 2000). Altogether, these mechanisms maintain a tight regulation of the mevalonate pathway activity and the intracellular concentration of cholesterol.

In addition to cholesterol, nonsterol isoprenoids, such as farnesyl pyrophosphate (FPP) and its derivative geranylgeranyl pyrophosphate (GGPP), are also produced by the mevalonate pathway. These isoprenoids are essential for the synthesis of key metabolites including ubiquinone and heme A, which are required for oxidative phosphorylation, and dolichol, which plays a role in N-glycosylation of proteins (Gruenbacher and Thurnher, 2017; Riscal et al., 2019; Waller et al., 2019). Isoprenoids are also indispensable for protein prenylation, which is essential for the membrane localization and activity of Ras and Ras-related GTP-binding proteins (Philips, 2012; Ridley, 2013; Sorrentino et al., 2014). Therefore, in addition to providing cholesterol as building blocks for membranes, the mevalonate pathway generates metabolites required for oncogenic activity. Accordingly, up-regulation of mevalonate pathway genes has been described in various cancer types, including breast and lung cancer, where it has been linked to p53 gain-of-function mutations (Freed-Pastor et al., 2012; Turrell et al., 2017).

Altered cholesterol metabolism has been implicated in PDAC, and targeting various components of this program has been shown to impair PDAC progression (Guillaumond et al., 2015; Kusama et al., 2002; Li et al., 2016; Liao et al., 2013). Additionally, overexpression of mevalonate pathway genes has been reported in both human PDAC and mouse models (Carrer et al., 2019; Cornell et al., 2019 *Preprint*; Deng et al., 2018; Guillaumond et al., 2015; Karasinska et al., 2020). However, the genetic drivers of this up-regulation in PDAC remain largely unknown. Moreover, considering that the mevalonate pathway is tightly regulated by cholesterol-mediated feedback inhibition, it is unclear how tumors maintain its hyperactivation. Indeed, despite enhanced SREBP2 activity, the mevalonate pathway, at the level of HMGCR activity and SREBP2 itself, would eventually be subject to the stringent feedback inhibition mediated by increased levels of cholesterol.

Here we used organoid and mouse models of PDAC to investigate the changes in cholesterol metabolism during tumor progression. Using various genetic approaches, we identified an essential role for SOAT1 in sustaining the hyperactivation of the mevalonate pathway to promote PDAC progression. SOAT1 restricts cholesterol accumulation, thus preventing feedback inhibition of the mevalonate pathway in PDAC cells with mutant p53 and p53 loss of heterozygosity (LOH).

Results

SOAT1 expression increases during PDAC progression

To determine how cholesterol metabolism changes across all stages of PDAC progression, we first sought to compare the expression of genes involved in cholesterol biosynthesis, homeostasis, transport, and catabolism in a panel of pancreatic organoids (Boj et al., 2015) generated from normal C57BL/6J pancreata (N organoids, n = 7), pancreatic intraepithelial neoplasia (PanIN) lesions (P organoids, n = 6) from the KC (*Kras*$^{LSL\text{-}G12D/+}$; *Pdx1*-Cre) mouse model of PDAC (Hingorani et al., 2003), as well as tumor (T organoids, n = 12) and metastatic (M organoids, n = 9) samples from the KPC (*Kras*$^{LSL\text{-}G12D/+}$; *Trp53*$^{LSL\text{-}R172H/+}$; *Pdx1*-Cre) mouse model of PDAC (Hingorani et al., 2005). RNA sequencing (RNA-seq) of these organoids revealed increased expression of genes involved in cholesterol biosynthesis in the M relative to the N, P, and T organoids (Fig. 1 A). Notably, we also observed significant up-regulation of SREBP2 (gene name *Srebf2*), the master regulator of the cholesterol biosynthetic pathway, in the M organoids (Fig. 1 A, Fig. S 1A, and Table S1). SREBP2 transcriptionally activates itself (Sato et al., 1996) and induces the expression of mevalonate pathway genes (Horton et al., 1998). Accordingly, shRNA-mediated down-regulation of SREBP2 in M organoids significantly reduced the expression of mevalonate pathway genes, such as *Hmgcr*, 3-hydroxy-3-methylglutaryl-CoA synthase 1 (*Hmgcs1*), farnesyl diphosphate synthase (*Fdps*), and squalene epoxidase (*Sqle*; Fig. S1 B). These observations suggest that the cholesterogenic gene expression differences observed across N, P, T, and M organoids are due to differential activation of SREBP2. Indeed, Western blot analysis confirmed a marked reduction in the inactive precursor form of SREBP2 (SREBP2-p) and an increase in the mature form of SREBP2 (SREBP2-m) in M organoids (Fig. 1 B), which reflects an increase in proteolytic maturation and activation of SREBP2 in these cells. Since SREBP2 is typically activated in response to low cholesterol levels (Riscal et al., 2019), we evaluated whether M organoids had lower intracellular cholesterol levels compared with N, P, and T organoids. Surprisingly, no difference was observed in unesterified cholesterol levels among these organoids (Fig. S1 C). Instead, M organoids had significantly more esterified cholesterol compared with N, P, and T organoids (Fig. 1 C). Furthermore, we found increased expression of the cholesterol esterification enzyme SOAT1 in M organoids, relative to N, P, and matched T organoids (Fig. 1, D and E; Fig. S1 D; and Table S1). These findings collectively show that increased cholesterol metabolism pathways during tumor progression in PDAC are not a response to intracellular cholesterol deficiency, but rather suggest the differential regulation of cholesterol homeostasis.

To determine whether similar changes accompany PDAC progression in vivo, we compared expression levels of SOAT1 in normal pancreas tissue, tumors from KC mice, and tumors and metastases from KPC mice. In contrast to the organoid models, where SOAT1 elevation was observed only in M, but not T,

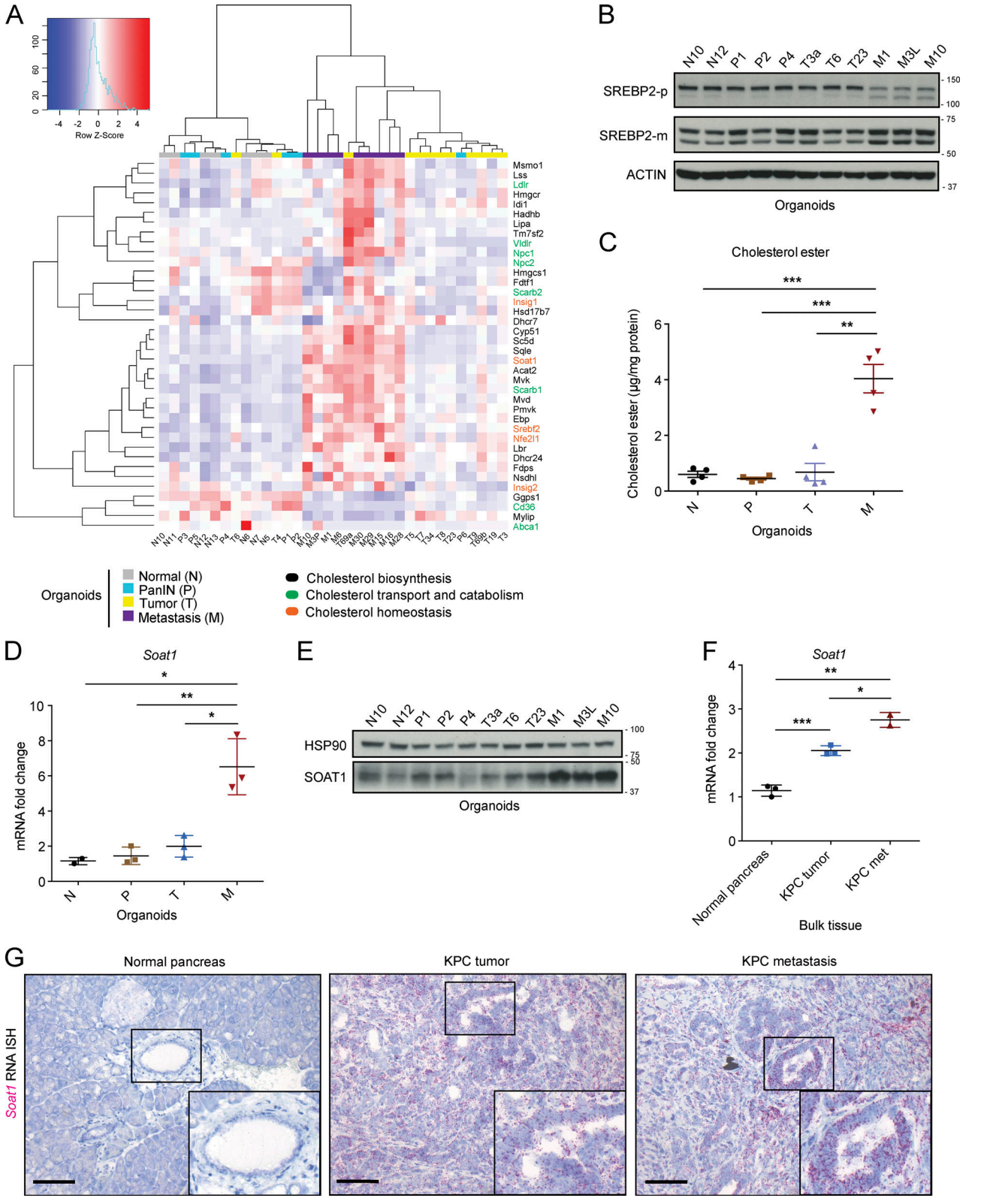

Figure 1. **SOAT1 expression increases during PDAC progression. (A)** RNA-seq analysis of murine normal N (n = 7), PanIN P (n = 6), tumor T (n = 12), and metastatic M (n = 9) pancreatic organoids showing genes involved in cholesterol biosynthesis (black), transport and catabolism (green), and homeostasis (orange). The color scheme of the heat map represents Z-score distribution. **(B)** Western blot analysis of the inactive SREBP2 precursor (SREBP2-p) and the mature SREBP2 protein (SREBP2-m) in a panel of N (n = 2), P (n = 3), T (n = 3), and tumor-matched M (n = 3) organoids. ACTIN, loading control. **(C)** Cholesterol ester assays for N (n = 4), P (n = 4), T (n = 4), and tumor-matched M (n = 4) organoids. Results show mean ± SEM of two biological replicates (two technical replicates each). **, P < 0.01; ***, P < 0.001, paired Student's t test. **(D)** qPCR analysis of *Soat1* in murine pancreatic N (n = 2), P (n = 3), T (n = 3), and tumor-

matched M (n = 3) organoids. Results show mean ± SEM. *, P < 0.05; **, P < 0.01, paired Student's t test between matched T and M organoids; unpaired Student's t test between N, P, and M organoids. **(E)** Western blot analysis of SOAT1 in N (n = 2), P (n = 3), T (n = 3), and tumor-matched M (n = 3) organoids shown in B. HSP90, loading control. **(F)** qPCR analysis of *Soat1* in C57BL/6J normal pancreata (n = 3), KPC tumors (n = 3), and KPC metastases (n = 2). Results show mean ± SEM. *, P < 0.05; **, P < 0.01; ***, P < 0.001, unpaired Student's t test. **(G)** Representative RNA ISH of *Soat1* in C57BL/6J normal pancreas (n = 3), KPC tumor (n = 3), and matched metastasis (n = 3). Inserts: magnification. Scale bars, 200 µm. Molecular weights in kilodaltons.

organoids in vivo, SOAT1 was significantly up-regulated in both KPC tumors and metastases compared with normal pancreata and KC tumors by quantitative PCR (qPCR), RNA in situ hybridization (ISH), and Western blot analysis (Fig. 1, F and G; and Fig. S1 E). *Srebf2* was also up-regulated in KPC tumors and metastases compared with normal pancreata as shown by RNA ISH (Fig. S1 F). Up-regulation of SOAT1 in human PDAC has been previously described (Li et al., 2016), and analysis of The Cancer Genome Atlas (TCGA) and Genotype-Tissue Expression datasets with the Gene Expression Profiling Interactive Analysis (GEPIA) tool (Tang et al., 2017) confirmed the up-regulation of *SOAT1*, *SREBF2*, and SREBP2 target genes (*LDLR* and *HMGCR*) in human PDAC compared with normal pancreas (Fig. S1 G). Altogether, these results show increased expression of SOAT1 and SREBP2-target genes in both murine and human PDAC.

SOAT1 expression is dependent on p53 status

Our in vitro results indicated increased SOAT1 expression in M organoids, whereas in vivo SOAT1 up-regulation occurred already in primary tumors. To resolve this discrepancy, we sought to determine the molecular mechanism behind the increase in SOAT1 levels in M organoids. We did not commonly observe recurrent amplification of *Soat1* in murine M organoids compared with N, P, and T organoids, as assessed by copy number variation analysis (Fig. 2 A). Next, we determined whether altered chromatin state might explain the increase in SOAT1 expression in M organoids. To that end, we analyzed a previously published dataset that used chromatin immunoprecipitation (ChIP) followed by DNA sequencing (ChIP-seq) to identify regions of histone H3 lysine 27 acetylation (H3K27ac) enrichment in matched murine T and M PDAC organoids (Roe et al., 2017). Within an enhancer (GAIN) region upstream of *Soat1*, H3K27ac levels were higher in M compared with T organoids (Fig. S2 A), suggesting that higher levels of active transcription may explain the increased SOAT1 expression in M organoids. Whereas SREBP2 is the canonical transcription factor associated with the cholesterol biosynthesis pathway, DNA motif analysis did not identify SREBP2 motifs in this region upstream of *Soat1* showing increased H3K27ac (Table S2). Additionally, shRNA-mediated SREBP2 down-regulation did not affect *Soat1* levels in T and M PDAC organoid lines (Fig. S2 B). Thus, SREBP2 is unlikely to promote activation of chromatin upstream of *Soat1* and enhanced transcription of *Soat1* in M organoids.

We previously showed that in our murine PDAC organoid cultures, most T organoids retain the WT copy of p53 (*Trp53*), whereas M organoids have undergone LOH to lose the WT copy of p53 (Boj et al., 2015). In contrast, the WT p53 allele is lost in PDAC tumors in vivo at both primary and metastatic sites, as indicated by stabilization of mutant p53 (Alexandrova et al., 2017), resulting in positive staining for this protein (Fig. S2 C). Indeed, p53 LOH has been demonstrated to be a feature of advanced PDAC in vivo (Baumgart et al., 2010; Filippini et al., 2019; Lüttges et al., 2001). We therefore evaluated whether differences in p53 status could underlie the differences in SOAT1 expression observed in vitro and in vivo. To this end, we analyzed SOAT1 levels in two PDAC organoid lines (T69A and T69B) that were isolated from distinct tumors in the same KPC mouse but differed in their p53 status. T69B retained the WT p53 allele, whereas T69A had undergone LOH of p53 (Fig. 2 B). As expected, LOH of p53 led to the stabilization of mutant p53 protein and to a decrease in WT p53 target genes in T69A organoids compared with T69B organoids (Fig. 2 C; and Fig. S2 D; Alexandrova et al., 2017). qPCR and Western blot analyses revealed significantly increased SOAT1 expression in T69A compared with T69B (Fig. 2, C and D), suggesting that p53 LOH could promote this up-regulation.

To validate these results, we isolated p53 LOH cells by treating two early-passage T organoid lines with 10 µM Nutlin-3a, which inhibits the interaction between the E3 ubiquitin-protein ligase MDM2 and p53 (Vassilev et al., 2004), leading to p53 activation and depletion of cells that retain the WT allele of p53. With this approach, we generated two pairs of matching T organoid lines, $p53^{R172H/WT}$ and $p53^{R172H/LOH}$ T organoids (Fig. S2 E). Transcriptional and protein analysis of these organoids showed increased SOAT1 expression following p53 LOH (Fig. 2, E and F; and Fig. S2 F). To validate whether SOAT1 up-regulation upon p53 LOH is linked to increased transcriptional activity in these organoid lines, we performed ChIP-seq of H3K27ac in T6 and T23 organoids with or without p53 LOH and observed higher H3K27ac levels in the GAIN region upstream of *Soat1* in the organoids with LOH of WT p53 (Fig. S2 G).

To further assess the role of mutant p53 in modulating SOAT1 expression, we used base editing, followed by Nutlin-3a treatment, to generate two pairs of isogenic lines of P organoids, $p53^{WT/WT}$ and $p53^{R270C/LOH}$ P organoids (Fig. 2 G and Fig. S2, H and I). The $p53^{R270C/LOH}$ organoids had increased SOAT1 levels relative to the $p53^{WT/WT}$ organoids, suggesting that p53 mutation and p53 LOH are sufficient to promote elevated SOAT1 expression (Fig. 2, H and I; and Fig. S2 J). Finally, we analyzed a panel of patient-derived PDAC organoids carrying either two copies of WT *TP53* or mutant *TP53* combined with LOH of WT *TP53* (Tiriac et al., 2018). Consistent with our results in murine PDAC organoids, we observed increased SOAT1 expression in human organoids with mutant *TP53*/LOH (Fig. 2, J and K).

Because p53 mutations can lead to gain-of-function phenotypes (Freed-Pastor and Prives, 2012), we sought to determine whether the increase in SOAT1 expression observed was due to the loss of tumor-suppressive WT p53 activity or to a gain-of-function of mutant p53. To this end, we established p53-null T organoids ($T^{-/-}$) from the KPPC ($Kras^{LSL\text{-}G12D/+}$; $Trp53^{lox/lox}$;

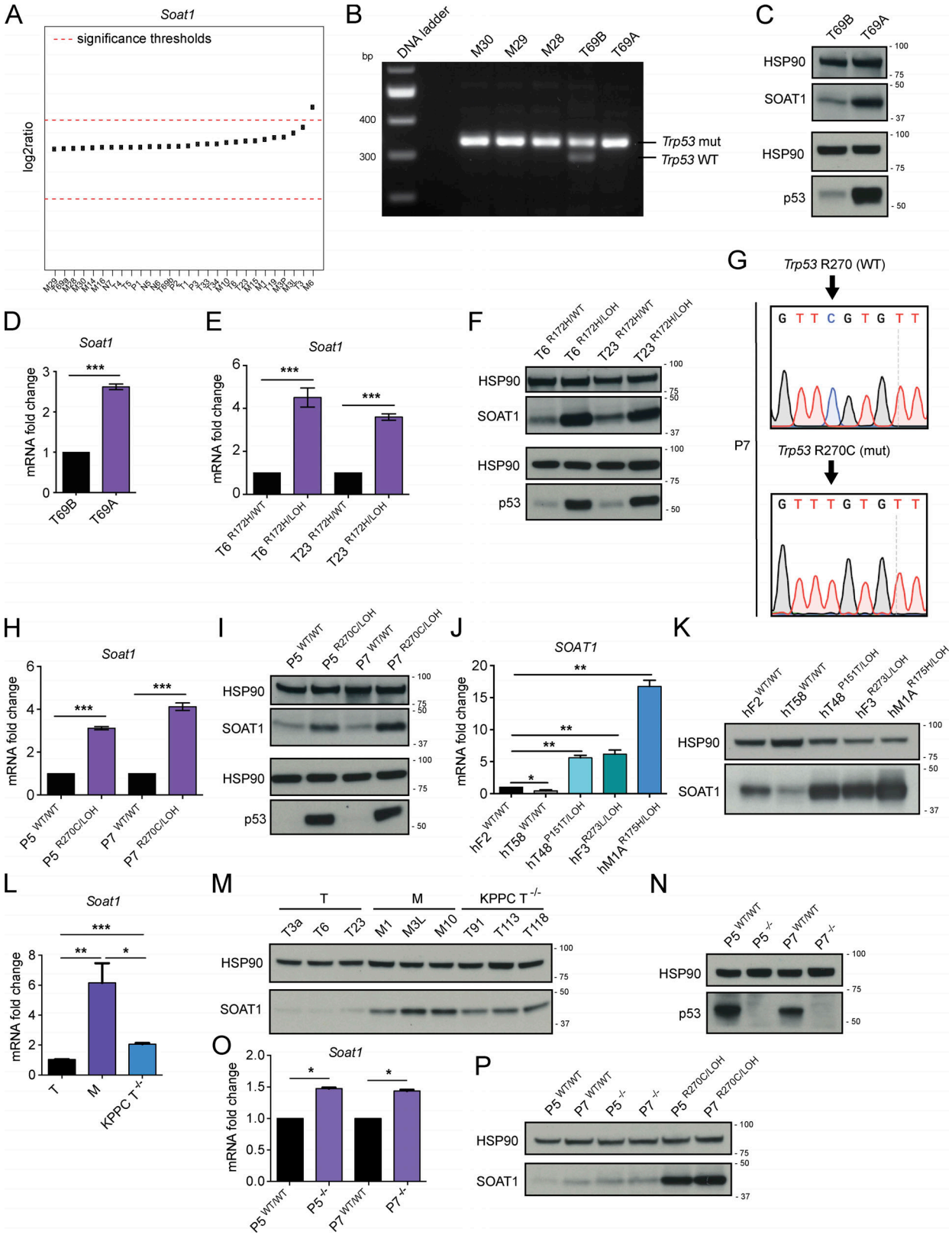

Figure 2. **SOAT1 expression is dependent on p53 status. (A)** Copy number variation analysis of *Soat1* in murine N (n = 3), P (n = 3), T (n = 11), and M (n = 11) pancreatic organoids. **(B)** DNA gel showing *Trp53* genetic status in metastatic (n = 3, M30, M29, and M28) and tumor (n = 2, T69B and T69A) PDAC organoids. T69B and T69A were generated from two primary tumors of the same KPC mouse. mut, mutant. **(C)** Western blot analysis of SOAT1 and p53 in T69B and T69A organoids (n = 2). HSP90, loading controls. **(D)** qPCR analysis of *Soat1* in T69A and T69B organoids. Results show mean ± SD of two technical replicates. ***, P < 0.001, paired Student's t test. **(E)** qPCR analysis of *Soat1* in T6 and T23 organoids with or without p53 LOH. Results show mean ± SD of two technical replicates. ***, P < 0.001, paired Student's t test. **(F)** Western blot analysis of SOAT1 and p53 in T6 and T23 organoids with or without p53 LOH. HSP90, loading

controls. **(G)** DNA sequencing results showing *Trp53* mutation following base-editing in P7 organoids. **(H)** qPCR analysis of *Soat1* in P5 and P7 organoids with $p53^{WT/WT}$ or $p53^{R270C/LOH}$. Results show mean ± SD of three technical replicates. ***, P < 0.001, paired Student's *t* test. **(I)** Western blot analysis of SOAT1 and p53 in P5 and P7 organoids with $p53^{WT/WT}$ or $p53^{R270C/LOH}$. HSP90, loading controls. **(J)** qPCR analysis of *SOAT1* in a panel of human PDAC organoids with either mutant or WT p53. Results show mean ± SD of three technical replicates. *, P < 0.05; **, P < 0.01, paired Student's *t* test. Human PDAC organoids were derived from resections of primary tumors (hT), fine needle aspirates/biopsies of primary tumors (hF) or metastases (hM). **(K)** Western blot analysis of SOAT1 in a panel of human PDAC organoids with either mutant or WT p53 ($n = 2$). HSP90, loading control. **(L)** qPCR analysis of *Soat1* in KPC T (T3a, T6, and T23) and M (M1, M3L, and M10) organoids and in KPPC $T^{-/-}$ (T91, T113, and T118) organoids. Results show mean ± SD of three biological replicates. *, P < 0.05; **, P < 0.01; ***, P < 0.001, unpaired Student's *t* test. **(M)** Western blot analysis of SOAT1 in T ($n = 3$), M ($n = 3$), and $T^{-/-}$ ($n = 3$) organoids. HSP90, loading control. **(N)** Western blot analysis of p53 in P5 and P7 organoids with $p53^{WT/WT}$ or $p53^{-/-}$. HSP90, loading control. **(O)** qPCR analysis of *Soat1* in P5 and P7 organoids with $p53^{WT/WT}$ or $p53^{-/-}$. Results show mean ± SD of two technical replicates. *, P < 0.05, paired Student's *t* test. **(P)** Western blot analysis of SOAT1 in P5 and P7 organoids with $p53^{WT/WT}$, $p53^{-/-}$ or $p53^{R270C/LOH}$. HSP90, loading control. Molecular weights in kilodaltons.

Pdx1-Cre) mouse model of PDAC (Bardeesy et al., 2006; Marino et al., 2000). We then compared SOAT1 expression in $T^{-/-}$ organoids to KPC T ($p53^{R172H/WT}$) and M ($p53^{R172H/LOH}$) organoids by qPCR and Western blot analyses. SOAT1 levels in KPPC organoids were intermediate between KPC T and M organoids (Fig. 2, L and M; and Fig. S2 K). Additionally, KO of WT *Trp53* in P organoids led to a modest up-regulation of SOAT1 expression in contrast to the high SOAT1 levels observed in P organoids harboring mutant p53 and p53 LOH (Fig. 2, N–P). These results show that loss of WT p53 contributes to increased SOAT1 expression, but to a lesser extent than the combined presence of mutant p53 and LOH of WT p53. To investigate whether mutant p53 directly regulate *Soat1* transcription, we depleted p53 in murine and human M organoids. shRNA-mediated down-regulation of p53 did not markedly reduce *Soat1* expression (Fig. S2, L–N), showing that mutant p53 is not required for continuous *Soat1* expression in PDAC. Altogether, our data indicate that although mutant p53 is required to induce elevated SOAT1 levels, sustained expression of mutant p53 is not necessary to maintain SOAT1 up-regulation. Notably, previous studies in breast cancer demonstrated the role of mutant p53 in directly regulating the transcription of mevalonate pathway genes (Freed-Pastor et al., 2012). In contrast, we found that mutant p53 depletion did not affect the expression of mevalonate pathway genes, such as *Hmgcr*, *Hmgcs1*, *Fdps*, and *Sqle*, in PDAC M organoids (Fig. S2 O). Altogether, these results support a role of mutant p53 in the induction of SOAT1 expression in PDAC cells that have undergone p53 LOH.

SOAT1 loss significantly impairs PDAC progression

Having established that SOAT1 expression is elevated in PDAC, we tested whether SOAT1 contributes to PDAC progression. We first assessed the effect of SOAT1 loss in PDAC organoids with p53 LOH. *Soat1* deletion by CRISPR/Cas9 in murine M3L metastatic organoids modestly attenuated cell proliferation in vitro (Fig. 3 A and Fig. S3 A). Likewise, shRNA-mediated down-regulation of *Soat1* modestly impaired the cell proliferation of T69A and $T6^{R172H/LOH}$ organoids (Fig. S3, B–F).

We then evaluated the effect of SOAT1 loss in vivo by orthotopic transplantation of M3L organoids with or without KO of *Soat1*. The loss of *Soat1* significantly impaired tumor growth and metastasis formation (Fig. 3, B–D; and Fig. S3, G and H) and extended the survival (Fig. 3 E) of these orthotopically grafted organoid (OGO) models. Similarly, shRNA-mediated targeting of *Soat1* in $T6^{R172H/LOH}$ OGO models significantly reduced tumor growth and metastasis formation (Fig. S3, I–M). Notably, the small tumors that developed from transplanted $T6^{R172H/LOH}$ organoids expressing an shRNA targeting *Soat1* reexpressed *Soat1* (Fig. S3 N), indicating that they escaped shRNA-mediated silencing in vivo. Altogether, these data corroborate previous studies in human xenografts (Li et al., 2016) and confirm that SOAT1 plays a central role in promoting PDAC progression in vivo.

We reasoned that the pronounced effect of SOAT1 loss on PDAC tumor growth could depend on the higher levels of cholesterol present in vivo compared with the concentration in cell culture media (Stechman et al., 2010). Therefore, we hypothesized that culturing organoids in cholesterol-replete conditions (Volkmar et al., 2019; Widenmaier et al., 2017) would recapitulate the in vivo phenotype. Indeed, culturing M3L organoids in the presence of 50 µM solubilized cholesterol (cholesterol media) enhanced the proliferation defect of the *Soat1* KO organoids compared with the more modest defect seen in complete media (Fig. 3, A and F; and Fig. S3 O). Accordingly, similar results were obtained for T69A organoids expressing an shRNA targeting *Soat1* (Fig. S3, D and P). Because, in vivo, cholesterol is primarily delivered to cells via lipoprotein complexes, we sought to determine whether the phenotype observed using solubilized cholesterol could be recapitulated with cholesterol-carrying LDL. As expected, *Soat1* loss also significantly impaired the proliferation of M3L organoids in complete media supplemented with 0.5% LDL (LDL media; Fig. S3 Q). These results suggest that SOAT1 is required for the proliferation of PDAC organoids that have already undergone p53 LOH in physiologically relevant, cholesterol-replete conditions.

p53 LOH sensitizes tumor cells to SOAT1 deficiency

We then investigated whether SOAT1 was also required for the proliferation of N, P, and $T^{R172H/WT}$ organoids. Interestingly, N organoids were unaffected by SOAT1 depletion, even when cultured in cholesterol media (Fig. S4, A–D). Moreover, whereas $T6^{R172H/WT}$ and $T23^{R172H/WT}$ organoids were unaffected by SOAT1 loss in both media conditions (Fig. 4 A and Fig. S4, E–H), the proliferation of the matched p53 LOH counterparts was significantly impaired, and more markedly so in cholesterol media (Fig. 4 B; Fig. S3, E and F; and Fig. S4, G, I, and J). We further confirmed the differential sensitivity to SOAT1 loss with respect to different p53 status in isogenic $p53^{WT/WT}$ and $p53^{R270C/LOH}$ P organoids. In both complete and cholesterol media, proliferation of $p53^{WT/WT}$ P organoids was unaffected by

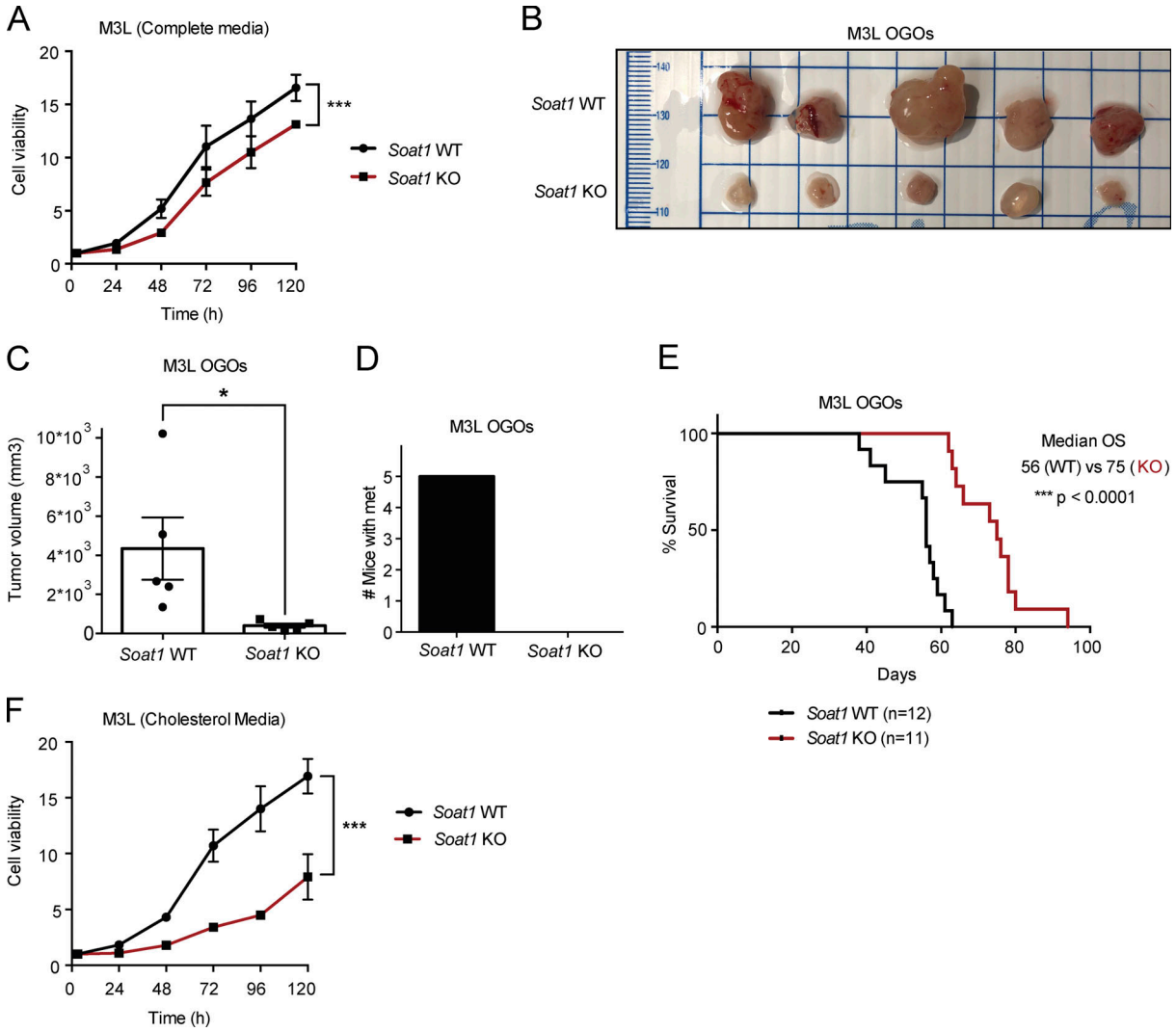

Figure 3. **SOAT1 loss significantly impairs PDAC progression. (A)** Proliferation curves of murine M3L organoids with *Soat1* WT or KO. Results show mean ± SD of five technical replicates. ***, P < 0.001, unpaired Student's *t* test calculated for the last time point. **(B)** Images of tumors derived from M3L OGO models with *Soat1* WT (*n* = 5) or KO (*n* = 5) in *nu/nu* mice on day 48 after transplantation. **(C)** Quantification of tumor volumes from B. Results show mean ± SEM of five biological replicates per cohort. *, P < 0.05, unpaired Student's *t* test. **(D)** Quantification of mice with metastases for the experiment shown in B. **(E)** Survival curves of M3L OGO models with *Soat1* WT (*n* = 12) or KO (*n* = 11) in *nu/nu* mice. ***, P < 0.001. OS, overall survival. **(F)** Proliferation curves of M3L organoids with *Soat1* WT or KO in complete media containing 50 µM cholesterol. Results show mean ± SD of five technical replicates. ***, P < 0.001, unpaired Student's *t* test calculated for the last time point.

Soat1 down-regulation (Fig. 4 C and Fig. S4, K–M). In contrast, the proliferation of $p53^{R270C/LOH}$ P organoids was significantly impaired by *Soat1* depletion, particularly in cholesterol media (Fig. 4 D and Fig. S4, N–P). Notably, despite the modest up-regulation of SOAT1, the proliferation of $T^{-/-}$ organoids was not significantly impaired by *Soat1* depletion in either media conditions (Fig. 4 E and Fig. S4, Q–S). Overall, our results indicate that the proliferation defect of SOAT1-deficient organoids is restricted to P, T, and M organoids with mutant p53 that have undergone LOH of the WT allele.

SOAT1 loss impaired the growth of tumors derived from PDAC organoids that underwent p53 LOH (Fig. 3, B–E; and Fig. S3, I–K). However, as SOAT1 depletion already affected the proliferation of these organoid lines in vitro, we could not exclude the possibility that the in vivo phenotype observed was due to intrinsic sensitivity of these organoids to SOAT1 loss, rather than due to the LOH of p53. The in vivo progression of tumors derived from $T^{R172H/WT}$ organoids has been shown to require the LOH of WT p53 (Filippini et al., 2019). Therefore, to further evaluate whether PDAC cell sensitivity to SOAT1 depletion is dependent on p53 LOH, we tested whether $T^{R172H/WT}$ organoids, whose proliferation is unaffected by SOAT1 depletion in vitro, acquire sensitivity to SOAT1 loss in vivo. To this end, we analyzed the effect of shRNA-mediated SOAT1 depletion in T8 organoids in vitro and in vivo. We first confirmed that T8 organoids retain the WT p53 in vitro and undergo p53 LOH in OGO tumors (Fig. S4, T and U). As expected, SOAT1 down-regulation did not affect the proliferation of T8 organoids in vitro (Fig. S4, V–X). In contrast, SOAT1 depletion in T8 OGO models completely suppressed tumor formation during the time the control

mice reached a humane endpoint (Fig. 4, F and G). Histological analysis of the pancreas of SOAT1-deficient T8 OGO models revealed the presence of small cystic lesions in two of five mice (Fig. 4 H), and RNA ISH analysis confirmed *Soat1* down-regulation at these sites compared with tumor controls (Fig. 4 I).

To further explore whether SOAT1 deficiency affects only the growth of PDAC tumors with mutant p53 and LOH of the WT allele, we analyzed T91$^{-/-}$ OGO models with or without shRNA-mediated SOAT1 down-regulation. In accordance with the in vitro results (Fig. 4 E and Fig. S4 S), SOAT1 down-regulation did not significantly affect tumor growth (Fig. 4, J–L) or metastasis formation (Fig. 4 M) of T91$^{-/-}$ OGO models. Overall, these results highlight the role of SOAT1 in promoting the proliferation of PDAC cells with mutant p53 that have undergone LOH of WT p53.

SOAT1 expression sustains the mevalonate pathway in PDAC

We hypothesized that the abrogation of cholesterol esterification upon SOAT1 loss would result in the accumulation of intracellular cholesterol, especially in cholesterol-replete conditions. As expected, assessment of esterified and unesterified cholesterol levels in M3L organoids showed a significant reduction of cholesterol esters and a significant increase in unesterified cholesterol in *Soat1* KO compared with *Soat1* WT organoids in both complete media and cholesterol media (Fig. 5, A and B). These results indicate that the proliferation defect observed in *Soat1* KO M3L organoids is associated with increased cholesterol accumulation.

To determine the mechanism underlying the proliferation defect observed upon SOAT1 loss in PDAC organoids that have undergone p53 LOH, we performed RNA-seq of M3L organoids with or without *Soat1* KO cultured in complete media and cholesterol media conditions for 24 h. At this time point, the organoid proliferation defect is not yet significant (Fig. 3, A and F) and, therefore, this analysis could enable the identification of pathways that are potentially the cause, rather than the consequence, of the impaired proliferation phenotype. RNA-seq analysis showed down-regulation of genes involved in cholesterol biosynthesis in *Soat1* KO M3L organoids compared with control organoids when cultured in cholesterol media (Fig. 5 C). Although modest, this down-regulation of cholesterol biosynthesis genes was also present in *Soat1* KO M3L organoids compared with control organoids when cultured in complete media (Fig. S5 A). These results are consistent with the presence of a more pronounced proliferation defect of *Soat1* KO M3L organoids in cholesterol media compared with complete media (Fig. 3, A and F). Accordingly, the cholesterol biosynthesis pathway was also down-regulated in *Soat1* KO M3L organoids cultured in cholesterol media compared with complete media (Fig. 5 D), whereas it was not significantly down-regulated in *Soat1* WT M3L organoids cultured in cholesterol media compared with complete media (Fig. S5 B). Additionally, Western blot analysis confirmed a decrease in SREBP2 activation in M3L organoids upon *Soat1* KO, as shown by the decrease of SREBP2 mature protein (SREBP2-m) in both culture conditions (Fig. 5 E). Altogether, these observations suggest that p53 LOH-dependent SOAT1 up-regulation supports the proliferation of M3L organoids by enabling these cells to evade the cholesterol-mediated feedback inhibition of SREBP2 activity.

Our analysis shows that loss of SOAT1 restores the cholesterol-mediated feedback inhibition of mevalonate pathway gene expression in PDAC cells with mutant p53 that have undergone p53 LOH. We then sought to determine whether SOAT1 loss also affects SREBP2 activity in cells that retain the WT copy of p53, and whose proliferation is not affected by SOAT1 depletion. In concordance with the results obtained in M3L organoids (Fig. S5 A), qPCR analysis of matched T6$^{R172H/WT}$ and T6$^{R172H/LOH}$ organoids cultured in complete media showed a decrease in the levels of SREBP2 target genes, including mevalonate pathway genes such as *Hmgcr*, *Hmgcs1*, *Fdps*, and *Sqle*, only in T6$^{R172H/LOH}$ organoids upon SOAT1 depletion (Fig. 5 F). Knockdown of SOAT1 led to a marked reduction in cholesterol esters and a clear increase in unesterified cholesterol in T6$^{R172H/LOH}$ organoids, whereas it only modestly affected the levels of esterified and unesterified cholesterol in T6$^{R172H/WT}$ organoids (Fig. S5, C and D). Finally, Western blot analysis confirmed a decrease in SREBP2 activation only in T6$^{R172H/LOH}$ organoids upon SOAT1 down-regulation when cultured in complete media, as shown by an increase in the inactive precursor form of SREBP2 (SREBP2-p) and a reduction of SREBP2-m, whereas no change was observed in T6$^{R172H/WT}$ organoids (Fig. 5 G). To determine whether this selective down-regulation of mevalonate pathway genes also occurred in cholesterol-replete conditions, we performed the above experiments in cholesterol media. We found that, in these conditions, SOAT1 down-regulation significantly decreased SREBP2 target genes and esterified cholesterol levels and led to a significant increase in unesterified cholesterol in both T6$^{R172H/WT}$ and T6$^{R172H/LOH}$ organoids (Fig. S5, E–G). Additionally, SOAT1 depletion decreased SREBP2 activity in T6$^{R172H/LOH}$ organoids more so than T6$^{R172H/WT}$ organoids, as shown by an increase in SREBP2-p and a modest reduction in SREBP2-m (Fig. S5 H). Because SOAT1 depletion selectively impaired the proliferation of p53 LOH organoids, these results suggest that p53 LOH organoids are selectively dependent on the mevalonate pathway.

The up-regulation of mevalonate pathway genes mediated by p53 loss or mutation has been shown to confer sensitivity to mevalonate pathway inhibition by statins in other cancer types (Freed-Pastor et al., 2012; Kaymak et al., 2020; Moon et al., 2019; Turrell et al., 2017). To determine whether increased dependency on the mevalonate pathway contributes to the differential sensitivity to SOAT1 loss in PDAC cells with p53 LOH compared with cells that retain WT p53, we treated T6$^{R172H/WT}$ and T23$^{R172H/WT}$ organoids and their matched p53 LOH counterparts with Simvastatin. Calculation of the half-maximal inhibitory concentration (IC_{50}) showed that T6$^{R172H/LOH}$ and T23$^{R172H/LOH}$ organoids were more sensitive to Simvastatin treatment than T6$^{R172H/WT}$ and T23$^{R172H/WT}$ organoid lines (Fig. 5 H). Similarly, M3L and T69A organoids were more sensitive than N and T69B organoids (Fig. S5 I), corroborating the observation that PDAC cells that have undergone p53 LOH are more dependent on the mevalonate pathway. To validate these findings, we depleted SREBP2 by shRNA-mediated knockdown in T organoids with or without p53 LOH. We confirmed that SREBP2 targeting led to

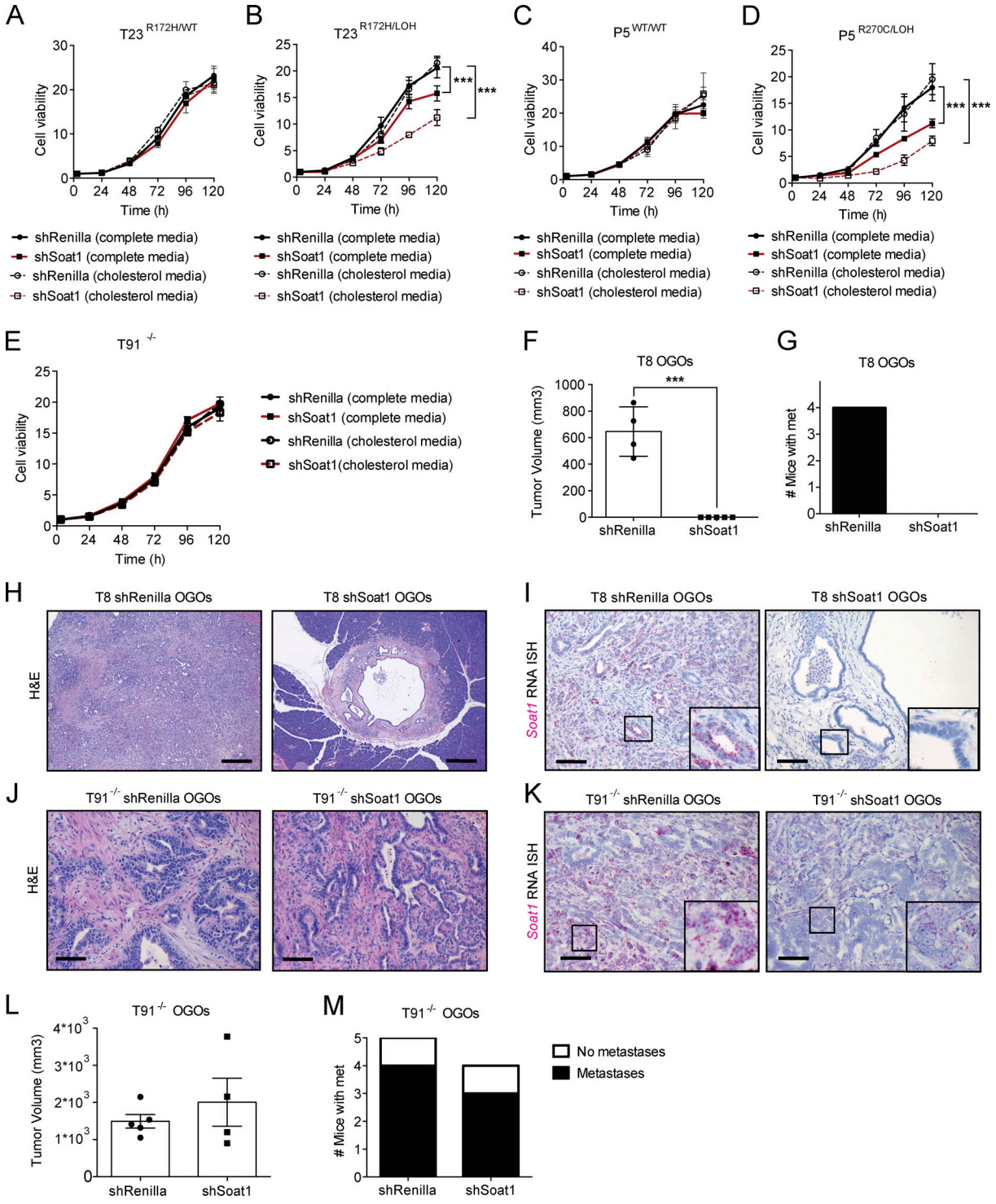

Figure 4. **p53 LOH sensitizes tumor cells to SOAT1 deficiency. (A)** Proliferation curves of $T23^{R172H/WT}$ organoids with or without expression of an shRNA targeting *Soat1* in complete media or complete media containing 50 µM cholesterol. Results show mean ± SD of five technical replicates. No statistical difference was found, as calculated by unpaired Student's *t* test for the last time point. **(B)** Proliferation curves of $T23^{R172H/LOH}$ organoids with or without expression of an shRNA targeting *Soat1* in complete media or complete media containing 50 µM cholesterol. Results show mean ± SD of five technical replicates. ***, P < 0.001, unpaired Student's *t* test calculated for the last time point. **(C)** Proliferation curves of $P5^{WT/WT}$ organoids with or without expression of an shRNA targeting *Soat1* in complete media or complete media containing 50 µM cholesterol. Results show mean ± SD of five technical replicates. No statistical difference was found, as calculated by unpaired Student's *t* test for the last time point. **(D)** Proliferation curves of $P5^{R270C/LOH}$ organoids with or without expression of an shRNA targeting *Soat1* in complete media or complete media containing 50 µM cholesterol. Results show mean ± SD of five technical replicates. ***, P < 0.001, unpaired Student's *t* test calculated for the last time point. **(E)** Proliferation curves of $T91^{-/-}$ organoids with or without expression of an shRNA targeting *Soat1* in complete media or complete media containing 50 µM cholesterol. Results show mean ± SD of five technical replicates. No statistical difference was found, as calculated by unpaired Student's *t* test for the last time point. **(F)** Quantification of tumor volumes of T8 OGO models with

(n = 5) or without (n = 4) expression of an shRNA targeting *Soat1* in NOD scid gamma mice on day 58 after transplantation. Results show mean ± SEM. ***, P < 0.001, unpaired Student's t test. **(G)** Quantification of mice with metastases for the experiment shown in F. **(H)** Representative H&E stain of T8 OGO models with or without expression of an shRNA targeting *Soat1* for the experiment shown in F (n = 2). Scale bars, 800 µm. **(I)** Representative RNA ISH of *Soat1* in T8 OGO models with or without expression of an shRNA targeting *Soat1* for the experiment shown in F (n = 2). Inserts: magnification. Scale bars, 200 µm. **(J)** Representative H&E stain of T91$^{-/-}$ OGO models with or without expression of an shRNA targeting *Soat1* in *nu/nu* mice on day 73 after transplantation (n = 2). Scale bars, 200 µm. **(K)** Representative RNA ISH of *Soat1* in T91$^{-/-}$ OGO models for the experiment shown in J (n = 2). Inserts: magnification. Scale bars, 200 µm. **(L)** Quantification of tumor volumes of T91$^{-/-}$ OGO models with (n = 4) or without (n = 5) expression of an shRNA targeting *Soat1* for the experiment shown in J. Results show mean ± SEM. No statistical difference was found, as calculated by unpaired Student's t test. **(M)** Quantification of mice with metastases for the experiment shown in L.

down-regulation of mevalonate pathway genes in both T$^{R172H/WT}$ and T$^{R172H/LOH}$ organoids (Fig. S5, J–M). Nonetheless, SREBP2 down-regulation only impaired the proliferation of T$^{R172H/LOH}$ organoids, whereas it did not affect T$^{R172H/WT}$ organoids (Fig. 5 I and Fig. S5 N). These results suggest that the differential effect of SOAT1 loss on the proliferation of PDAC cells is linked to the selective dependency on the mevalonate pathway in cells with p53 LOH.

We demonstrated that SOAT1 loss significantly down-regulates the expression of mevalonate pathway genes and impairs the proliferation of PDAC organoids with LOH of WT p53. We therefore hypothesized that the proliferation defect observed is a direct consequence of the disruption of oncogenic processes downstream of the mevalonate pathway. In addition to cholesterol, the mevalonate pathway generates a number of other metabolites, whose depletion could impair PDAC cell proliferation. Among these metabolites, nonsterol isoprenoids, such as FPP and GGPP, are required for protein prenylation. Prenylation of RAS and RHO proteins, which have been implicated in cancer progression, regulates their membrane localization and, consequently, their activity (Clark et al., 2000; Philips, 2012; Ridley, 2013; Sorrentino et al., 2014). We therefore tested whether SOAT1 loss leads to a reduction of the membrane localization of small G proteins, such as RAS, RHO (A, B, and C), RAC1, and CDC42. To this end, we performed membrane fractionation of M3L organoids with or without *Soat1* KO in complete media and cholesterol media conditions (Fig. S5, O and P). Our results showed a reduction in membrane-associated RAS and RHO levels upon *Soat1* KO, whereas changes in RAC1 and CDC42 levels were not apparent (Fig. 5 J). Additionally, phosphorylation of ERK, which is downstream of RAS activation, was also down-regulated upon SOAT1 loss (Fig. S5 Q). Importantly, addition of 25 µM FPP completely rescued the impaired proliferation of *Soat1* KO M3L organoids cultured in complete media (Fig. S5 R), and partially rescued their proliferation defect in cholesterol-replete conditions (Fig. 5 K). Furthermore, the addition of FPP in cholesterol media restored the levels of membrane RAS in M3L *Soat1* KO organoids (Fig. 5 L), supporting the hypothesis that the decrease in membrane localization of RAS in these cells is due to depletion of isoprenoids. In contrast, addition of FPP in cholesterol-replete conditions did not restore membrane RHO levels (Fig. 5 L), which may explain the partial rescue observed in the proliferation of M3L *Soat1* KO organoids (Fig. 5 K). Our results demonstrate that the proliferation defect observed upon SOAT1 loss in PDAC cells with p53 LOH is due to the down-regulation of the mevalonate pathway which, in turn, diminishes the levels of isoprenoids required for oncogenic signaling and optimal proliferation of these cells.

Taken together, these observations suggest that SOAT1 up-regulation enables PDAC cells with p53 LOH to evade the cholesterol-mediated feedback inhibition of the mevalonate pathway to promote oncogenic signaling and tumor progression.

Discussion

Negative feedback mechanisms maintain homeostasis in biological systems, and disruption of these regulatory mechanisms can trigger oncogenic transformation or drive malignant progression (Courtois-Cox et al., 2006; Zhao et al., 2015). Despite the stringent negative feedback exerted on the mevalonate pathway by unesterified cholesterol, mevalonate pathway genes are commonly up-regulated in cancer (Freed-Pastor et al., 2012; Kaymak et al., 2020; Moon et al., 2019; Turrell et al., 2017). How cancer cells escape cholesterol feedback inhibition to hyperactivate the mevalonate pathway is poorly understood. Our work directly addresses this standing question. Here, we find that the combination of p53 mutation and p53 LOH promotes cholesterol esterification by increasing SOAT1 expression, thereby enabling RAS-driven PDAC cells to evade cholesterol-mediated feedback inhibition to support their mevalonate pathway dependency (Fig. 6). In particular, SOAT1 upholds the SREBP2-driven cholesterogenic program in p53 LOH PDAC cells to sustain the production of nonsterol isoprenoids, such as FPP and GGPP, required for the activity of RAS and RHO proteins. Indeed, the addition of FPP mitigates the proliferation defect induced by SOAT1 loss, although only partial rescue was observed in cholesterol-replete media conditions. This result could be because, in these conditions, FPP cannot substitute for some of the functions performed by GGPP. For instance, whereas RAS is preferentially prenylated with FPP (Casey and Seabra, 1996; Whyte et al., 1997), RHOA is exclusively modified with GGPP (Zhang and Casey, 1996). Accordingly, the addition of FPP restored RAS membrane levels, but not RHO membrane levels. Additionally, GGPP is required for the synthesis of ubiquinone and dolichol (Hooff et al., 2010), and depletion of these metabolites may contribute to the proliferation defect observed. In support of this, a recent study demonstrated that inhibition of the mevalonate pathway induced apoptosis in p53-deficient colon cancer cells by decreasing ubiquinone levels, thereby impairing the synthesis of pyrimidine nucleotides (Kaymak et al., 2020). Finally, the incomplete rescue observed in cholesterol-replete media may be because excess cholesterol can induce cytotoxicity by generating ER stress (Fu et al., 2012; Maxfield and Tabas, 2005).

Here, we find a role of mutant p53 in promoting high expression of SOAT1 in PDAC. In lung cancer mouse models, the

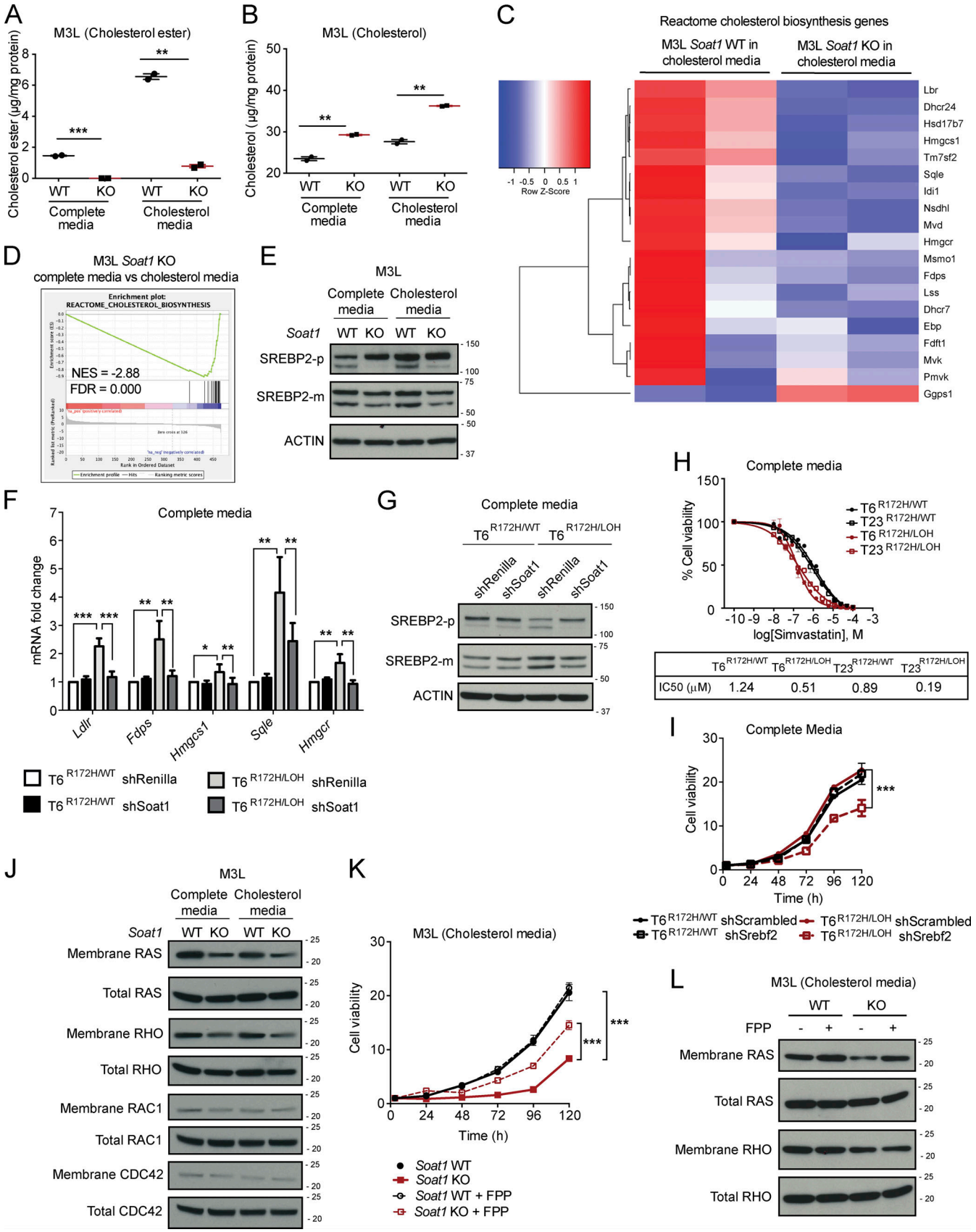

Figure 5. **SOAT1 expression sustains the mevalonate pathway in PDAC. (A)** Cholesterol ester assays for M3L organoids with *Soat1* WT or KO in complete media or complete media containing 50 µM cholesterol for 4 h. Results show mean ± SD of two technical replicates. **, P < 0.01; ***, P < 0.001, paired Student's *t* test. **(B)** Cholesterol assays for M3L organoids with *Soat1* WT or KO in complete media or complete media containing 50 µM cholesterol for 4 h.

Results show mean ± SD of two technical replicates. **, P < 0.01, paired Student's *t* test. **(C)** RNA-seq analysis of M3L organoids with *Soat1* WT (*n* = 2) or KO (*n* = 2) in complete media containing 50 µM cholesterol for 24 h showing genes involved in cholesterol biosynthesis. The color scheme of the heat map represents Z-score distribution. **(D)** GSEA plot for cholesterol biosynthesis in M3L organoids with *Soat1* KO in complete media or complete media containing 50 µM cholesterol for 24 h. NES, normalized enrichment score. **(E)** Western blot analysis of the inactive SREBP2 precursor (SREBP2-p) and the mature SREBP2 protein (SREBP2-m) in M3L organoids with or without *Soat1* KO in complete media or complete media containing 50 µM cholesterol for 24 h (*n* = 2). ACTIN, loading control. **(F)** qPCR analysis of *Ldlr*, *Fdps*, *Hmgcs1*, *Sqle*, and *Hmgcr* in $T6^{R172H/WT}$ and $T6^{R172H/LOH}$ organoids with or without expression of an shRNA targeting *Soat1* in complete media for 24 h. Results show mean ± SD of three technical replicates. *, P < 0.05; **, P < 0.01; ***, P < 0.001, paired Student's *t* test. **(G)** Western blot analysis of the inactive SREBP2 precursor (SREBP2-p) and the mature SREBP2 protein (SREBP2-m) in $T6^{R172H/WT}$ and $T6^{R172H/LOH}$ organoids with or without expression of an shRNA targeting *Soat1* in complete media for 24 h (*n* = 2). ACTIN, loading control. **(H)** IC_{50} curves and values of $T6^{R172H/WT}$, $T6^{R172H/LOH}$, $T23^{R172H/WT}$, and $T23^{R172H/LOH}$ organoids in complete media for 72 h with 1×10^{-10} M to 1×10^{-4} M Simvastatin. Results show mean ± SD of five technical replicates. **(I)** Proliferation curves of $T6^{R172H/WT}$ and $T6^{R172H/LOH}$ organoids with or without expression of an shRNA targeting *Srebf2* in complete media. Results show mean ± SD of five technical replicates. ***, P < 0.001, unpaired Student's *t* test calculated for the last time point. **(J)** Western blot analysis of membrane and total RAS, RHO (A, B, and C), RAC1, and CDC42 in M3L organoids with or without *Soat1* KO in complete media or complete media containing 50 µM cholesterol for 48 h (*n* = 2). **(K)** Proliferation curves of M3L organoids with *Soat1* WT or KO in complete media containing 50 µM cholesterol with or without 25 µM FPP. Results show mean ± SD of five technical replicates. ***, P < 0.001, unpaired Student's *t* test calculated for the last time point. **(L)** Western blot analysis of membrane and total RAS and RHO (A, B, and C) in M3L organoids with or without *Soat1* KO in complete media containing 50 µM cholesterol with or without 25 µM FPP for 48 h (*n* = 2). Molecular weights in kilodaltons.

expression of SOAT2, a paralog of SOAT1, is up-regulated in R270C p53 mutant cancer cells, but not in R172H p53 mutant or null cells (Turrell et al., 2017). In contrast, our results show that although SOAT1 is up-regulated in p53-null PDAC cells, SOAT1 levels are substantially lower compared with cells with either R270C or R172H p53 mutations and LOH of p53 WT. These observations are consistent with a model in which WT p53 suppresses SOAT1 expression, and mutant p53 promotes it. Accordingly, Andrysik et al. (2017) identified SOAT1 as an indirect target of transcriptional repression by WT p53 in breast cancer cells. Moreover, mutant p53 has been shown to regulate transcription by direct interaction with other transcription factors (Di Agostino et al., 2006; Freed-Pastor et al., 2012). However, this is unlikely to fully explain the role of mutant p53 in driving SOAT1 expression in PDAC, because sustained expression of mutant p53 was not required to maintain SOAT1 levels in M organoids. The exact mechanism underlying the increased expression of SOAT1 by mutant p53 remains to be determined.

Several lines of evidence have shown that the disruption of the mevalonate pathway by statins has potent anti-tumor effects in vitro. Additionally, although not corroborated in all analyses, some epidemiological studies indicate that statin treatment may reduce pancreatic cancer risk (Archibugi et al., 2019; Hamada et al., 2018a,b; Zhang et al., 2019). However, clinical trials evaluating the efficacy of statins in cancer have not been successful. These disappointing results have been largely attributed to the fact that statins primarily affect cholesterol biosynthesis in the liver, which leads to reduced circulating levels of cholesterol (Blumenthal, 2000; Ness et al., 1998). Low levels of cholesterol-carrying plasma lipoprotein particles limit the uptake of extracellular cholesterol by cancer cells, thus triggering compensatory activation of SREBP2 and cholesterol biosynthesis. Therefore, statin treatment in vivo paradoxically hyperactivates, rather than inhibits, the mevalonate pathway in cancer cells (Longo et al., 2019; Mo et al., 2019). We propose SOAT1-selective inhibitors as an alternative strategy to disrupt the aberrant mevalonate pathway activation in PDAC. Importantly, *Soat1* KO mice are viable and demonstrate intact hepatic and intestinal cholesterol metabolism (Meiner et al., 1996), since SOAT2 is the predominant cholesterol acyltransferase in these tissues (Anderson et al., 1998; Cases et al., 1998; Oelkers et al., 1998). Additionally, our work demonstrates that SOAT1 ablation selectively impairs the proliferation of PDAC cells with p53 LOH, a hallmark of advanced malignant progression (Baumgart et al., 2010; Filippini et al., 2019; Lüttges et al., 2001), but does not affect the proliferation of normal and preneoplastic pancreatic cells that have retained a copy of WT p53. Altogether, the presence of this synthetic vulnerability suggests a potential therapeutic window for selective inhibition of SOAT1 in PDAC.

Notably, the increased expression of mevalonate pathway genes is a feature of various cancer types (Carrer et al., 2019; Freed-Pastor et al., 2012; Guillaumond et al., 2015; Kaymak et al., 2020; Moon et al., 2019; Turrell et al., 2017) and, in addition to PDAC (Li et al., 2016), SOAT1 has been implicated in the progression of prostate (Yue et al., 2014) and hepatocellular (Jiang et al., 2019) carcinomas. Therefore, the role of SOAT1 in enabling cancer cell evasion from cholesterol feedback inhibition could be a common targetable vulnerability in cancer.

Materials and methods

Mouse models

C57BL/6J background (>20 backcrosses) KC ($Kras^{LSL\text{-}G12D/+}$; *Pdx1*-Cre), KPC ($Kras^{LSL\text{-}G12D/+}$; $Trp53^{LSL\text{-}R172H/+}$; *Pdx1*-Cre), and KPPC ($Kras^{LSL\text{-}G12D/+}$; $Trp53^{lox/lox}$; *Pdx1*-Cre) mice were previously described (Bardeesy et al., 2006; Hingorani et al., 2003, 2005; Marino et al., 2000). C57BL/6J (stock number 000664) and NOD scid gamma (stock number 005557) mice were purchased from the Jackson Laboratory; *nu/nu* mice (stock number 24102242) were purchased from the Charles River Laboratory. All animal procedures and studies were conducted in accordance with the Institutional Animal Care and Use Committee at Cold Spring Harbor Laboratory.

In vivo orthotopic transplantations

Injections for the generation of OGO models were conducted as previously described (Boj et al., 2015). Typically, 2.5×10^5 cells prepared from organoid cultures were resuspended as a 45-µl suspension of 50% Matrigel in PBS and injected into the

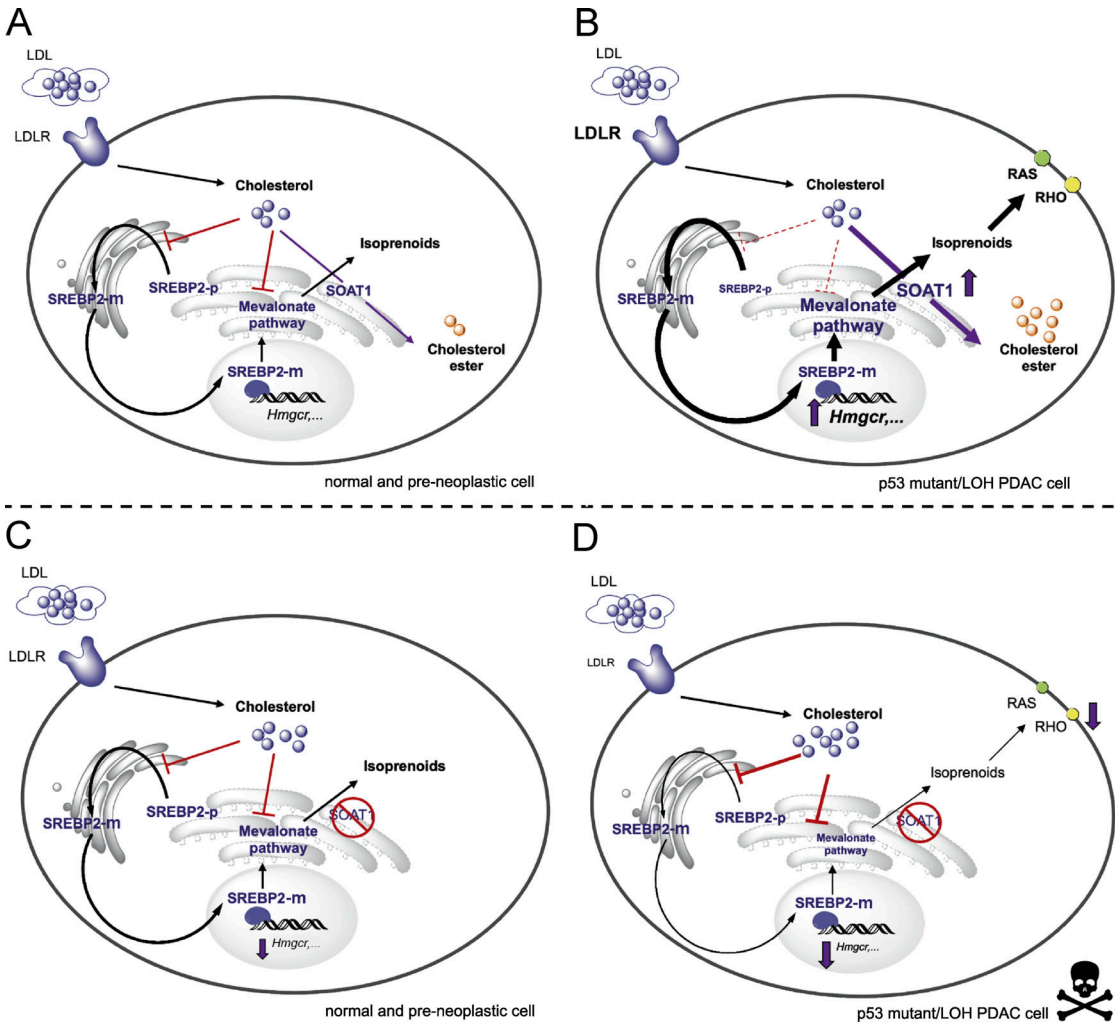

Figure 6. **SOAT1 abrogates cholesterol feedback inhibition to promote mevalonate pathway dependency in PDAC.** Model illustrating the role of SOAT1 in sustaining the activity of the mevalonate pathway. **(A and B)** Typically, compared with normal and preneoplastic pancreatic cells (A), SOAT1 levels, SREBP2 activity, and the expression of mevalonate pathway genes are up-regulated in PDAC cells with mutant p53 and LOH of WT p53 (B). **(C and D)** SOAT1 abrogation and consequential mevalonate pathway inhibition do not affect the proliferation of normal and preneoplastic pancreatic cells (C), whereas they significantly impair the proliferation of PDAC cells with mutant p53 that have undergone p53 LOH (D). SREBP2-p, inactive SREBP2 precursor. SREBP2-m, mature SREBP2 protein.

pancreas. For the survival study, mice were taken when they reached a humane endpoint.

Cell sorting of cancer cells

For sorting of cancer cells, T8 OGO tumors were processed as previously described (Biffi et al., 2019). Cells were stained for 30 min with anti-mouse CD45-Alexa Fluor 647 (103124; BioLegend), CD326 (EpCAM)-Alexa Fluor 488 (118212; BioLegend), CD31-Alexa Fluor 647 (102416; BioLegend), and PDPN-APC/Cy7 (127418; BioLegend) and for 15 min with DAPI. DAPI/CD45/CD31/PDPN$^-$ EpCAM$^+$ cells were sorted on the FACSAria cell sorter (BD) and processed for PCR-based genotyping of *Trp53* 1loxP.

Cell lines and cell culture

N, P, T, and M murine and human pancreatic organoid lines were cultured as previously described (Boj et al., 2015). All human organoid experiments were reviewed and approved by the Institutional Review Board of Cold Spring Harbor Laboratory and conducted in accordance with recognized ethical guidelines (Declaration of Helsinki). Murine organoids were generated as previously described (Boj et al., 2015). All cells were cultured at 37°C with 5% CO_2. Cell line authentication was not performed. *Mycoplasma* testing with the MycoAlert Mycoplasma Detection Kit (LT07-318; Lonza) is performed monthly at our institution, and each cell line has been tested at least once after thawing or isolation, and retested before RNA-seq and orthotopic transplantation experiments. To isolate the p53 LOH cells, early-passage T6 and T23 organoids were cultured in complete media with 10 µM Nutlin-3a (SML0580-5MG; Sigma-Aldrich) and propagated for three passages.

Cholesterol assay

Total cholesterol and unesterified cholesterol were measured using the manufacturer's protocol of a Cholesterol Quantitation

kit (MAK043, Sigma-Aldrich) and normalized to the total protein level measured by Bradford Assay. Amount of cholesterol esters were determined by subtracting the amount of unesterified cholesterol from total cholesterol.

PCR-based genotyping of *Trp53* 1loxP

Organoids were harvested and centrifuged at 4,000 rpm for 5 min at 4°C. Genomic DNA from freshly isolated tumor cells or organoids was extracted with DNEasy Blood & Tissue Kit (Qiagen) following the protocol for cultured cells. Each PCR reaction for *Trp53* 1loxP genotyping was performed in a 20-µl mixture containing 1× AmpliTaq Gold 360 master mix (Thermo Fisher Scientific), 0.5 µM each primer, and 40 ng template DNA. The following primers were used for genotyping: forward, 5′-AGC CTGCCTAGCTTCCTCAGG-3′; reverse, 5′-CTTGGAGACATAGCC ACACTG-3′ (Olive et al., 2004). The PCR cycling conditions were 95°C for 5 min, followed by 40 cycles at 95°C for 30 s, 56°C for 30 s, and 72°C for 30 s, with a final extension step at 72°C for 5 min. PCR products were separated on a 2% agarose gel in 1× TAE buffer. Gel imaging was performed with a Syngene UV transilluminator.

CRISPR/Cas9 KO and shRNA-mediated down-regulation

To knock out *Soat1*, Lenti-Cas9-puromycin plasmids were used. Organoids were infected and selected using 2.5 µg/ml puromycin (A1113803; Thermo Fisher Scientific). Single guide RNAs (sgRNAs) were designed using CRISPR Design and cloned into the LRGN (Lenti-sgRNA-EFS-GFP-neo) plasmid. Cleavage was confirmed using the GeneArt Genomic Cleavage Detection Kit (A24372; Invitrogen). Organoids were infected and plated as single cells in the presence of neomycin (10131035; Invitrogen). Knockout was confirmed by Sanger sequencing (not depicted) and Western blot analysis. To knock out *Trp53* in P organoids, two guides (gRNA 1: 5′-CACCGTGCCATGGAGGAGTCACAGT-3′; gRNA 2: 5′-CACCGAACAGATCGTCCATGCAGTG-3′) were designed to knock out *Trp53* by dual targeting of exons 2 and 4. These guides were cloned into the LRNG vector and lentivirally introduced into P5 and P7 organoids. 48 h after neomycin selection, organoids were passaged and then treated with 10 µM Nutlin-3a for three passages to select for $p53^{-/-}$ organoids. KO was confirmed by Western blot analysis. To knock down *Soat1*, an shRNA targeting *Soat1* (5′-TTGAACTCAAGTACCAGCCTTC-3′) was cloned into the LEPG vector (miR-E backbone), as previously described (Fellmann et al., 2013). Organoids were then retrovirally infected with *Soat1* shRNA and selected with 2 µg/ml puromycin 24 h after infection. A shRNA targeting *Renilla* luciferase (5′-TAGATAAGCATTATAATTCCTA-3′) was used as control (miR-E backbone). To knock down *Trp53*, an shRNA targeting *Trp53* (p53.1224; 5′-TGTATTACACATGTACTTGTAGTG G-3′) was inserted into a miR-30 backbone driven by the MSCV promoter (Premsrirut et al., 2011). A shRNA targeting *Renilla* luciferase (5′-TAGATAAGCATTATAATTCCTA-3′) was used as control (miR-30 backbone). To knock down *TP53*, previously described pRETRO-SUPER (pRS) constructs containing shRNAs targeting human *TP53* or a control (Brummelkamp et al., 2002) were used. To knock down *Srebf2*, TRC vectors were acquired from Horizon Discovery (Srebf2 #1: 5′-TTTAAGAAGTAGCTA GCCAAG-3′; Srebf2 #2: 5′-AATGAACAAGGCTTAGTCAGG-3′), and a scrambled shRNA was used as control.

Base editing

P organoids were dissociated into single cells, and 100,000 cells were transfected using the Amaxa electroporation system (Amaxa) with 1 µg base editor (CMV-BE3; Komor et al., 2016) and 500 ng ipUSEPR (Ruscetti et al., 2018) constructs containing a sgRNA targeting *Trp53* (5′-GTTCGTGTTTGTGCCTGCCC-3′) to induce a R270C mutation. Organoids were then plated in Matrigel and cultured in complete media for 24 h before addition of 2 µg/ml puromycin to select for organoids successfully transfected with the sgRNA. 48 h after puromycin selection, organoids were passaged and then treated with 10 µM Nutlin-3a for three passages to select for $p53^{R270C/LOH}$ organoids.

qPCR analysis

Typically, RNA (1 µg) was reverse transcribed using TaqMan reverse transcription reagents (N808-0234; Applied Biosystems). qPCR was performed using gene-specific TaqMan probes (Applied Biosystems) and master mix (4440040; Applied Biosystems). Gene expression was normalized to *Hprt*.

Membrane fractionation

Membrane fractionation was performed as previously described (Baghirova et al., 2015). Briefly, organoids were recovered from Matrigel with Cell Recovery Solution (354253, Corning). Organoid pellets were washed twice in PBS and permeabilized with a digitonin-based buffer. After a 10-min incubation at 4°C with constant mixing, permeabilized cells were centrifuged, and pellets containing the membrane fractions were solubilized in a NP-40–based lysis buffer and frozen until use. For Western blot analysis, 10 or 100 µg of protein was loaded for the membrane and total fractions, respectively.

Western blot analysis

Organoids were harvested in Cell Recovery Solution (Corning) and incubated with rotating for 1 h at 4°C. Cells were pelleted and lysed in 0.1% Triton X-100, 15 mmol/liter NaCl, 0.5 mmol/liter EDTA, and 5 mmol/liter Tris, pH 7.5, supplemented with protease inhibitors (11836170001; Roche) and a phosphatase inhibitor cocktail (4906845001; Roche). Cells were incubated on ice for 30 min before clarification. To prepare lysates for immunoblotting of SREBP2, organoids were harvested with Cell Recovery Solution and washed with cold PBS. After centrifugation, cells were lysed with radioimmunoprecipitation assay buffer with protease inhibitors and then sonicated at 4°C for intervals of 30 s for a total of five cycles. Standard procedures were used for Western blotting. Western blot analysis of SOAT1 requires incubation of the protein lysate at 70°C rather than at boiling temperature. Ponceau staining (P7170; Sigma-Aldrich) was performed before blocking. Primary antibodies used were SOAT1 (sc-20951, Santa Cruz), SREBP2 (ab30682, Abcam), HSP90α (07-2174; EMD Millipore), ACTIN (8456; Cell Signaling Technology), phosphorylated ERK (4370, Cell Signaling Technology), ERK (9102, Cell Signaling Technology), E-CADHERIN (3195, Cell Signaling Technology), p53 (P53-CM5P-L, Leica),

CDC42 (ACD03, Cytoskeleton), RAC1 (ARC03, Cytoskeleton), RHO (ab40673, Abcam), and RAS (3965, Cell Signaling Technology). Proteins were detected using HRP-conjugated secondary antibodies (Jackson ImmunoResearch Laboratories).

Proliferation assays and IC_{50} experiments

Organoids were first dissociated into single cells. 2,000 cells were then seeded in 10% Matrigel and the indicated media with 10 µM ROCK inhibitor (Y27632, Selleck Chem) on white 96-well plates precoated with a 70% Matrigel/PBS bed. Cell viability was measured every 24 h for 5 d with Cell Titer Glo (G7573, Promega), per manufacturer's instructions, on a SpectraMax I3 (Molecular Devices) plate reader. For cholesterol media, 50 µM cholesterol solubilized in methyl β cyclodextrin (Sigma-Aldrich; C4951) was added to complete media. For LDL media, 0.5% LDL concentrate (5354, Cone Bio) was added to complete media. For rescue with FPP, 25 µM FPP (F6892; Sigma-Aldrich) was added to complete media. For drug treatment experiments, organoids were plated as described above. Simvastatin (1612700; Sigma-Aldrich) at a concentration range from 10^{-10} M to 10^{-4} M was added 24 h after plating. After 96 h, cell viability was measured with Cell Titer Glo, and IC_{50} values for Simvastatin were computed using Prism (GraphPad).

Immunohistochemical staining and RNA ISH

Standard procedures were used for immunohistochemistry (IHC) with a primary antibody for p53 (NCL-L-p53-CM5p; Leica). Hematoxylin was used as nuclear counterstain. H&E and Masson's trichrome staining were performed according to standard protocols. RNA ISH was performed using the manufacturer's protocol (RNAscope 322360; Advanced Cell Diagnostics) and probes specific for *Soat1* (541821; Advanced Cell Diagnostics) or *Srebf2* (562261; Advanced Cell Diagnostics).

RNA-seq preparation and analysis

Samples were collected in 1 ml of TRIzol reagent (15596-018; Thermo Fisher Scientific). RNA was extracted using the PureLink RNA Mini Kit (12183018A; Thermo Fisher Scientific) per manufacturer's instructions. RNA quality was assessed on a 2100 Bioanalyzer Instrument (Agilent) using the RNA 6000 Nano Kit (5067-1511; Agilent). Only RNAs with RNA integrity numbers >9 were used for RNA-seq. A TruSeq Stranded Total RNA Kit with RiboZero Human/Mouse/Rat (RS-122-2201 and RS-122-2202; Illumina) was used for library construction using 1 µg RNA per sample, per manufacturer's instructions. Library quality was assessed using a 2100 Bioanalyzer Instrument (Agilent) using the High Sensitivity DNA Kit (5067-4626; Agilent), and concentration was assessed using a Qubit (ThermoFisher Scientific) with the dsDNA HS Assay Kit (Q32854; Thermo Fisher Scientific). Libraries were sequenced (101 bp paired-end + 7 bp barcode reads) at the Cold Spring Harbor Laboratory Next Generation Sequencing Shared Resource using an Illumina NextSeq500 (high output flow cell).

For RNA-seq of N, P, T, and M organoids, read quality was first quantified using FastQC v0.11.8 (Babraham Bioinformatics). Reads were mapped to transcript annotation GENCODE M22 (Frankish et al., 2019) corresponding to mouse genome GRCm38.p6 using STAR v2.6.0c (Dobin et al., 2013). RSEM v1.3.1 (Li and Dewey, 2011) was used to extract counts per gene. First, a prefiltering step was performed to remove genes expressed in fewer than two samples. Identification of batch- and sex-related variables was then performed using Bioconductor package sva v3.32.1 (Leek et al., 2012). Those two surrogate variables have been added to the DESeq2 design formula. Differential gene expression analysis was performed using Bioconductor package DESeq2 v1.24.0 (Love et al., 2014). Genes with false discovery rate (FDR) < 0.05 and log2 fold change ≥ 1 were identified as differentially expressed genes. The normalized counts per gene were also obtained from DESeq2. The differential gene expression analysis between metastasis and tumor represents the unique case of paired analysis. For this analysis, only one metastasis and one tumor originating from the same mouse were randomly retained. As all samples came from the same batch, no batch correction was needed. The mouse pairing information was included in the DESeq2 design formula. The RNA-seq data for the M organoids are available at the Gene Expression Omnibus (GEO) under accession no. GSE142467. The RNA-seq data for the N, P, and T organoids are available at GEO under accession no. GSE63348.

For M3L organoids with or without *Soat1* KO, RNA-seq libraries were mapped to GENCODE GRCm38 primary assembly using STAR (v2.7.3), and gene expression estimations were performed using RSEM (v1.2.29). DESeq2 (v1.22.2) was used for identifying differentially expressed genes with default parameters. Genes with adjusted P values <0.05 were selected as significant genes. Pathway enrichment analysis was conducted using gene set enrichment analysis (GSEA; v3.0) program and canonical pathway collections available in MSigDB based on significantly differentially expressed genes. Customized R scripts were used for plotting. These RNA-seq data are available at GEO under accession no. GSE141737.

Organoid copy number variation analysis

The whole-genome sequencing data are available at the Sequence Read Archive under accession no. PRJNA599977. Copy number on mouse organoids was inferred as previously described (Kendall and Krasnitz, 2014). Low-coverage whole-genome sequences were aligned with Bowtie v1.2.3 (Langmead and Salzberg, 2012) and Samtools v1.9 on mm10 genome partitioned into 5,000 bins beforehand. The results were post-processed with CNprep version 2.0 to calculate the copy numbers relative to their central values for each segment. The threshold to assign an alteration was calculated as 3× the quantiles 0.025 (deletion) and 0.975 (amplification) of the log2ratio for normal organoids. When the absolute value was <0.2, we replaced it by 0.2. The obtained thresholds are 0.20 (amplification) and −0.36 (deletion).

H3K27ac ChIP-sequencing for $T^{R172H/WT}$ and $T^{R172H/LOH}$ organoids

Organoids were grown as described above and harvested in 2 mg/ml dispase II (17105041; Thermo Fisher Scientific) for 20 min at 37°C. Cells were cross-linked with 1% formaldehyde for 10 min at room temperature and then quenched with 0.125 M

glycine for 5 min. Cells were washed three times in PBS, resuspended in SDS buffer (50 mM Tris-HCl, pH 8, 2% SDS, 100 mM NaCl, and 5 mM EDTA, with protease and phosphatase inhibitors) and stored at −80°C before further processing for ChIP. Cells were pelleted by centrifugation and suspended in 0.5 ml of IP buffer (100 mM Tris-HCl, pH 8.5, 0.3% SDS, 1.7% Triton X-100, 100 mM NaCl, 5 mM EDTA, and protease and phosphatase inhibitors). Cells were disrupted by sonication for two cycles (15 min, low amplitude) using Bioruptor (Diagenode), yielding genomic DNA fragments with a bulk size of 100–400 bp. After sonication, chromatin was centrifuged at 14,000 rpm for 10 min at 4°C, and immunoprecipitation was performed with 0.5 ml of precleared chromatin and 3 µg of antibody against H3K27ac (ab4729; Abcam) prebound to G-protein–coupled paramagnetic beads (10004D; Dynabeads) in 0.5% BSA/PBS. After overnight incubation at 4°C with rotation, beads were washed six times with a modified radioimmunoprecipitation assay buffer (50 mM Hepes, pH 7.6, 500 mM LiCl, 1 mM EDTA, 1% NP-40, and 0.7% Na-deoxycholate) and a final wash with TE containing 50 mM NaCl. DNA was eluted in 250 µl elution buffer (2% SDS in TE buffer), and cross-links were reversed by incubation overnight at 65°C. DNA was then purified by Qiaquick columns (Qiagen) and quantified using PicoGreen (P11496; Thermo Fisher Scientific). 10 ng ChIP DNA was prepared for Illumina sequencing with TruSeq ChIP Sample Prep Kit (Illumina) following the manufacturer's instructions. Libraries were quality checked using a Bioanalyzer 2100 (Agilent) with a High Sensitivity DNA Kit and quantified using PicoGreen. Equimolar amounts of libraries were pooled and subjected to single-read, 75-bp sequencing using an Illumina NextSeq 500 platform. For ChIP-seq analysis, raw reads were mapped to mouse mm10 genome using Bowtie2 software using sensitive settings (Langmead and Salzberg, 2012). Duplicate reads were removed after alignment. Peaks were identified using MACS2 software using 5% FDR cutoff and broad peak option (Feng et al., 2012). Sequencing depth normalized ChIP-seq pileup tracks were generated using the UCSC genome browser (Kent et al., 2002). H3K27ac GAIN enhancer regions were obtained from Roe et al. (2017) and converted to mm10 coordinates using UCSC LiftOver tool. H3K27ac ChIP-seq for $T^{R172H/WT}$ and $T^{R172H/LOH}$ organoids are available at GEO under accession no. GSE144704. H3K27ac ChIP-seq datasets in N, P, T, and M organoids were from Roe et al. (2017).

SREBP2 DNA motif analysis

H3K27ac GAIN regions were obtained from Roe et al. (2017). Relative H3K27ac signal fold change of each region was calculated from comparing geometric means of six M organoids and six T organoids. Regions having more than twofold enrichments were selected for motif scanning. In the end, 757 of 857 regions were kept, including one region located upstream (~30 Kbp) of *Soat1*. DNA sequences of selected regions were obtained using the getfasta program available in BEDTools suit from UCSC mm9 genome assembly. Because of the lack of murine *Srebf2* DNA motifs available, *SREBF2* (MA0596.1) human motif weight matrix was downloaded from the JASPAR transcription factor binding database (v2020). Fimo program from MEME suit was used for motif scanning with significant P value $<1 \times 10^{-5}$.

Statistical analysis

GraphPad Prism was used for graphical representation of data. Statistical analysis was performed using Student's *t* test.

Online supplemental material

Fig. S1 contains data corroborating SOAT1 and SREBP2 increased expression during PDAC progression. Fig. S2 contains data corroborating that SOAT1 expression is dependent on p53 mutation and LOH in PDAC. Fig. S3 contains data showing that SOAT1 loss significantly impairs PDAC progression. Fig. S4 contains data supporting that the combination of p53 mutation and LOH sensitizes tumor cells to SOAT1 loss. Fig. S5 contains data corroborating a role of SOAT1 in sustaining the mevalonate pathway in PDAC. Table S1 contains the normalized expected counts for the RNA-seq analysis of murine pancreatic N, P, T, and M organoids shown in Fig. 1 and Fig. S1. Table S2 contains the DNA motif analysis performed using the *SREBF2* (MA0596.1) human motif.

Acknowledgments

This work was performed with assistance from the Cold Spring Harbor Laboratory shared resources, which are supported by the National Institutes of Health (Cancer Center Support Grant 5P30CA045508: Bioinformatics, DNA Sequencing, Flow Cytometry, Animal, and Animal and Tissue Imaging Shared Resources). The authors are supported by National Institutes of Health (Cancer Center Support Grant 5P30CA045508) and the Lustgarten Foundation, where D.A. Tuveson is a distinguished scholar and Director of the Lustgarten Foundation–designated Laboratory of Pancreatic Cancer Research. D.A. Tuveson is also supported by the Thompson Foundation, the Cold Spring Harbor Laboratory and Northwell Health Affiliation, the Northwell Health Tissue Donation Program, the Cold Spring Harbor Laboratory Association, and the National Institutes of Health (5P30CA45508, U01CA210240, R01CA229699, U01CA224013, 1R01CA188134, and 1R01CA190092). This work was also supported by a gift from the Simons Foundation (552716 to D.A. Tuveson and C.R. Vakoc). S.W. Lowe is an investigator at the Howard Hughes Medical Institute and is the Geoffrey Beene Chair of Cancer Biology. C.R. Vakoc was also supported by Pershing Square Sohn Cancer Research Alliance, the Cold Spring Harbor Laboratory and Northwell Health Affiliation, the National Cancer Institute (5P01CA013106 and 1RO1CA229699), the Thompson Family Foundation, and a Career Development Award from the Pancreatic Cancer Action Network-American Association for Cancer Research (16-20-25-VAKO). A. Krasnitz was supported by funding from the Simons Center for Quantitative Biology at Cold Spring Harbor Laboratory. G. Biffi was a fellow of the Human Frontier Science Program (LT000195/2015-L) and European Molecular Biology Organization (ALTF 1203-2014). T.D.D. Somerville was supported by a grant from the State of New York (C150158). C. Tonelli was a fellow of the American-Italian Cancer Foundation. F.J. Sánchez-Rivera is an Howard Hughes Medical Institute Hanna Gray Fellow and was partially supported by an Memorial Sloan Kettering Cancer Center Translational Research Oncology Training Fellowship (National

Institutes of Health T32-CA160001). L.A. Baker was supported through the National Institutes of Health (F32CA192904). C-I. Hwang was supported by the National Cancer Institute (F32CA180717 and K22CA226037). Y. Park is supported by the National Cancer Institute (R50CA211506). The results shown here are in part based on data generated by the TCGA Research Network (http://www.cancer.gov/tcga). The Genotype-Tissue Expression Project was supported by the Common Fund of the Office of the Director of the National Institutes of Health, and by National Cancer Institute, National Human Genome Research Institute, National Heart, Lung, and Blood Institute, National Institute on Drug Abuse, National Institute of Mental Health, and National Institute of Neurological Disorders and Stroke. The data used for the analyses described in this manuscript were obtained from the GEPIA tool.

Author contributions: Conceptualization: T.E. Oni and G. Biffi. Investigation: T.E. Oni, G. Biffi, L.A. Baker, C. Tonelli, T.D.D. Somerville, C-I. Hwang, H. Cox, R.P. Lumia, and K. Khaledi. Methodology: T.E. Oni and G. Biffi. Formal analysis and interpretation of data: T.E. Oni, G. Biffi, Y. Hao, A. Deschênes, P. Belleau, E. Brosnan, and A. Doshi. Visualization: T.E. Oni and G. Biffi. Writing – original draft: T.E. Oni and G. Biffi. Writing – review & editing: T.E. Oni, G. Biffi and D.A. Tuveson. Project administration: Y. Park. Resources: F.J. Sánchez-Rivera. Supervision: D.A. Tuveson, C.R. Vakoc, A. Krasnitz, S.W. Lowe, and L.C. Trotman. Funding acquisition: D.A. Tuveson.

Disclosures: C. Vakoc reported personal fees from KSQ Therapeutics outside the submitted work. D.A. Tuveson reported "other" from Leap Therapeutics, Surface Oncology, and Cygnal Therapeutics; grants from ONO and Fibrogen; and personal fees from Merck outside the submitted work. D.A. Tuveson is a SAB member and stock holder of Leap Therapeutics, Surface Oncology, and Cygnal, has a research project with ONO and Fibrogen, and is a consultant for Merck. None of this work related to the publication. No other disclosures were reported.

Submitted: 21 December 2019
Revised: 28 March 2020
Accepted: 12 May 2020

References

Alexandrova, E.M., S.A. Mirza, S. Xu, R. Schulz-Heddergott, N.D. Marchenko, and U.M. Moll. 2017. p53 loss-of-heterozygosity is a necessary prerequisite for mutant p53 stabilization and gain-of-function in vivo. *Cell Death Dis.* 8. e2661. https://doi.org/10.1038/cddis.2017.80

Anderson, R.A., C. Joyce, M. Davis, J.W. Reagan, M. Clark, G.S. Shelness, and L.L. Rudel. 1998. Identification of a form of acyl-CoA:cholesterol acyltransferase specific to liver and intestine in nonhuman primates. *J. Biol. Chem.* 273:26747–26754. https://doi.org/10.1074/jbc.273.41.26747

Andrysik, Z., M.D. Galbraith, A.L. Guarnieri, S. Zaccara, K.D. Sullivan, A. Pandey, M. MacBeth, A. Inga, and J.M. Espinosa. 2017. Identification of a core TP53 transcriptional program with highly distributed tumor suppressive activity. *Genome Res.* 27:1645–1657. https://doi.org/10.1101/gr.220533.117

Archibugi, L., P.G. Arcidiacono, and G. Capurso. 2019. Statin use is associated to a reduced risk of pancreatic cancer: A meta-analysis. *Dig. Liver Dis.* 51: 28–37. https://doi.org/10.1016/j.dld.2018.09.007

Baghirova, S., B.G. Hughes, M.J. Hendzel, and R. Schulz. 2015. Sequential fractionation and isolation of subcellular proteins from tissue or cultured cells. *MethodsX.* 2:440–445. https://doi.org/10.1016/j.mex.2015.11.001

Bardeesy, N., A.J. Aguirre, G.C. Chu, K.H. Cheng, L.V. Lopez, A.F. Hezel, B. Feng, C. Brennan, R. Weissleder, U. Mahmood, et al. 2006. Both p16(Ink4a) and the p19(Arf)-p53 pathway constrain progression of pancreatic adenocarcinoma in the mouse. *Proc. Natl. Acad. Sci. USA.* 103: 5947–5952. https://doi.org/10.1073/pnas.0601273103

Baumgart, M., M. Werther, A. Bockholt, M. Scheurer, J. Rüschoff, W. Dietmaier, B.M. Ghadimi, and E. Heinmöller. 2010. Genomic instability at both the base pair level and the chromosomal level is detectable in earliest PanIN lesions in tissues of chronic pancreatitis. *Pancreas.* 39: 1093–1103. https://doi.org/10.1097/MPA.0b013e3181dc62f6

Biffi, G., T.E. Oni, B. Spielman, Y. Hao, E. Elyada, Y. Park, J. Preall, and D.A. Tuveson. 2019. IL1-Induced JAK/STAT Signaling Is Antagonized by TGFβ to Shape CAF Heterogeneity in Pancreatic Ductal Adenocarcinoma. *Cancer Discov.* 9:282–301. https://doi.org/10.1158/2159-8290.CD-18-0710

Blumenthal, R.S.. 2000. Statins: effective antiatherosclerotic therapy. *Am. Heart J.* 139:577–583. https://doi.org/10.1016/S0002-8703(00)90033-4

Boj, S.F., C.I. Hwang, L.A. Baker, I.I. Chio, D.D. Engle, V. Corbo, M. Jager, M. Ponz-Sarvise, H. Tiriac, M.S. Spector, et al. 2015. Organoid models of human and mouse ductal pancreatic cancer. *Cell.* 160:324–338. https://doi.org/10.1016/j.cell.2014.12.021

Brown, M.S., and J.L. Goldstein. 1997. The SREBP pathway: regulation of cholesterol metabolism by proteolysis of a membrane-bound transcription factor. *Cell.* 89:331–340. https://doi.org/10.1016/S0092-8674(00)80213-5

Brummelkamp, T.R., R. Bernards, and R. Agami. 2002. Stable suppression of tumorigenicity by virus-mediated RNA interference. *Cancer Cell.* 2: 243–247. https://doi.org/10.1016/S1535-6108(02)00122-8

Carrer, A., S. Trefely, S. Zhao, S.L. Campbell, R.J. Norgard, K.C. Schultz, S. Sidoli, J.L.D. Parris, H.C. Affronti, S. Sivanand, et al. 2019. Acetyl-CoA Metabolism Supports Multistep Pancreatic Tumorigenesis. *Cancer Discov.* 9:416–435. https://doi.org/10.1158/2159-8290.CD-18-0567

Cases, S., S. Novak, Y.W. Zheng, H.M. Myers, S.R. Lear, E. Sande, C.B. Welch, A.J. Lusis, T.A. Spencer, B.R. Krause, et al. 1998. ACAT-2, a second mammalian acyl-CoA:cholesterol acyltransferase. Its cloning, expression, and characterization. *J. Biol. Chem.* 273:26755–26764. https://doi.org/10.1074/jbc.273.41.26755

Casey, P.J., and M.C. Seabra. 1996. Protein prenyltransferases. *J. Biol. Chem.* 271:5289–5292. https://doi.org/10.1074/jbc.271.10.5289

Clark, E.A., T.R. Golub, E.S. Lander, and R.O. Hynes. 2000. Genomic analysis of metastasis reveals an essential role for RhoC. *Nature.* 406:532–535. https://doi.org/10.1038/35020106

Coates, H.W., and A.J. Brown. 2019. A wolf in sheep's clothing: unmasking the lanosterol-induced degradation of HMG-CoA reductase. *J. Lipid Res.* 60: 1643–1645. https://doi.org/10.1194/jlr.C119000358

Cornell, L.G., S. Peri, D. Restifo, A. Klochkova, T.R. Hartman, A.M. O'Reilly, R. Francescone, J. Franco-Barraza, N. Shah, E. Nicolas, et al. 2019. Cholesterol deprivation induces TGFβ signaling to promote basal differentiation in pancreatic cancer. *bioRxiv* https://www.biorxiv.org/content/10.1101/633719v2.full (Preprint posted May 11, 2019)

Courtois-Cox, S., S.M. Genther Williams, E.E. Reczek, B.W. Johnson, L.T. McGillicuddy, C.M. Johannessen, P.E. Hollstein, M. MacCollin, and K. Cichowski. 2006. A negative feedback signaling network underlies oncogene-induced senescence. *Cancer Cell.* 10:459–472. https://doi.org/10.1016/j.ccr.2006.10.003

Deng, Y.Z., Z. Cai, S. Shi, H. Jiang, Y.R. Shang, N. Ma, J.J. Wang, D.X. Guan, T.W. Chen, Y.F. Rong, et al. 2018. Cilia loss sensitizes cells to transformation by activating the mevalonate pathway. *J. Exp. Med.* 215: 177–195. https://doi.org/10.1084/jem.20170399

Di Agostino, S., S. Strano, V. Emiliozzi, V. Zerbini, M. Mottolese, A. Sacchi, G. Blandino, and G. Piaggio. 2006. Gain of function of mutant p53: the mutant p53/NF-Y protein complex reveals an aberrant transcriptional mechanism of cell cycle regulation. *Cancer Cell.* 10:191–202. https://doi.org/10.1016/j.ccr.2006.08.013

Dobin, A., C.A. Davis, F. Schlesinger, J. Drenkow, C. Zaleski, S. Jha, P. Batut, M. Chaisson, and T.R. Gingeras. 2013. STAR: ultrafast universal RNA-seq aligner. *Bioinformatics.* 29:15–21. https://doi.org/10.1093/bioinformatics/bts635

Endo, A.. 1992. The discovery and development of HMG-CoA reductase inhibitors. *J. Lipid Res.* 33:1569–1582.

Fellmann, C., T. Hoffmann, V. Sridhar, B. Hopfgartner, M. Muhar, M. Roth, D.Y. Lai, I.A. Barbosa, J.S. Kwon, Y. Guan, et al. 2013. An optimized microRNA backbone for effective single-copy RNAi. *Cell Rep.* 5: 1704–1713. https://doi.org/10.1016/j.celrep.2013.11.020

Feng, J., T. Liu, B. Qin, Y. Zhang, and X.S. Liu. 2012. Identifying ChIP-seq enrichment using MACS. *Nat. Protoc.* 7:1728–1740. https://doi.org/10.1038/nprot.2012.101

Filippini, D., S. Agosto, P. Delfino, M. Simbolo, G. Piro, B. Rusev, L. Veghini, C. Cantù, F. Lupo, S. Ugel, et al. 2019. Immunoevolution of mouse pancreatic organoid isografts from preinvasive to metastatic disease. *Sci. Rep.* 9:12286. https://doi.org/10.1038/s41598-019-48663-7

Frankish, A., M. Diekhans, A.M. Ferreira, R. Johnson, I. Jungreis, J. Loveland, J.M. Mudge, C. Sisu, J. Wright, J. Armstrong, et al. 2019. GENCODE reference annotation for the human and mouse genomes. *Nucleic Acids Res.* 47(D1):D766–D773. https://doi.org/10.1093/nar/gky955

Freed-Pastor, W.A., and C. Prives. 2012. Mutant p53: one name, many proteins. *Genes Dev.* 26:1268–1286. https://doi.org/10.1101/gad.190678.112

Freed-Pastor, W.A., H. Mizuno, X. Zhao, A. Langerød, S.H. Moon, R. Rodriguez-Barrueco, A. Barsotti, A. Chicas, W. Li, A. Polotskaia, et al. 2012. Mutant p53 disrupts mammary tissue architecture via the mevalonate pathway. *Cell.* 148:244–258. https://doi.org/10.1016/j.cell.2011.12.017

Fu, S., S.M. Watkins, and G.S. Hotamisligil. 2012. The role of endoplasmic reticulum in hepatic lipid homeostasis and stress signaling. *Cell Metab.* 15:623–634. https://doi.org/10.1016/j.cmet.2012.03.007

Ghosh, S., R.W. St Clair, and L.L. Rudel. 2003. Mobilization of cytoplasmic CE droplets by overexpression of human macrophage cholesteryl ester hydrolase. *J. Lipid Res.* 44:1833–1840. https://doi.org/10.1194/jlr.M300162-JLR200

Gruenbacher, G., and M. Thurnher. 2017. Mevalonate metabolism governs cancer immune surveillance. *OncoImmunology.* 6. e1342917. https://doi.org/10.1080/2162402X.2017.1342917

Guillaumond, F., G. Bidaut, M. Ouaissi, S. Servais, V. Gouirand, O. Olivares, S. Lac, L. Borge, J. Roques, O. Gayet, et al. 2015. Cholesterol uptake disruption, in association with chemotherapy, is a promising combined metabolic therapy for pancreatic adenocarcinoma. *Proc. Natl. Acad. Sci. USA.* 112:2473–2478. https://doi.org/10.1073/pnas.1421601112

Halbrook, C.J., and C.A. Lyssiotis. 2017. Employing Metabolism to Improve the Diagnosis and Treatment of Pancreatic Cancer. *Cancer Cell.* 31:5–19. https://doi.org/10.1016/j.ccell.2016.12.006

Hallin, J., L.D. Engstrom, L. Hargis, A. Calinisan, R. Aranda, D.M. Briere, N. Sudhakar, V. Bowcut, B.R. Baer, J.A. Ballard, et al. 2020. The $KRAS^{G12C}$ Inhibitor MRTX849 Provides Insight toward Therapeutic Susceptibility of KRAS-Mutant Cancers in Mouse Models and Patients. *Cancer Discov.* 10:54–71. https://doi.org/10.1158/2159-8290.CD-19-1167

Hamada, T., N. Khalaf, C. Yuan, A. Babic, V. Morales-Oyarvide, Z.R. Qian, J.A. Nowak, K. Ng, P. Kraft, D.A. Rubinson, et al. 2018a. Statin use and pancreatic cancer risk in two prospective cohort studies. *J. Gastroenterol.* 53:959–966. https://doi.org/10.1007/s00535-018-1430-x

Hamada, T., N. Khalaf, C. Yuan, V. Morales-Oyarvide, A. Babic, J.A. Nowak, Z.R. Qian, K. Ng, D.A. Rubinson, P. Kraft, et al. 2018b. Prediagnosis Use of Statins Associates With Increased Survival Times of Patients With Pancreatic Cancer. *Clin. Gastroenterol. Hepatol.* 16:1300–1306.e3. https://doi.org/10.1016/j.cgh.2018.02.022

Hingorani, S.R., E.F. Petricoin, A. Maitra, V. Rajapakse, C. King, M.A. Jacobetz, S. Ross, T.P. Conrads, T.D. Veenstra, B.A. Hitt, et al. 2003. Preinvasive and invasive ductal pancreatic cancer and its early detection in the mouse. *Cancer Cell.* 4:437–450. https://doi.org/10.1016/S1535-6108(03)00309-X

Hingorani, S.R., L. Wang, A.S. Multani, C. Combs, T.B. Deramaudt, R.H. Hruban, A.K. Rustgi, S. Chang, and D.A. Tuveson. 2005. Trp53R172H and KrasG12D cooperate to promote chromosomal instability and widely metastatic pancreatic ductal adenocarcinoma in mice. *Cancer Cell.* 7:469–483. https://doi.org/10.1016/j.ccr.2005.04.023

Hooff, G.P., W.G. Wood, W.E. Müller, and G.P. Eckert. 2010. Isoprenoids, small GTPases and Alzheimer's disease. *Biochim. Biophys. Acta.* 1801:896–905. https://doi.org/10.1016/j.bbalip.2010.03.014

Horton, J.D., J.L. Goldstein, and M.S. Brown. 2002. SREBPs: activators of the complete program of cholesterol and fatty acid synthesis in the liver. *J. Clin. Invest.* 109:1125–1131. https://doi.org/10.1172/JCI0215593

Horton, J.D., I. Shimomura, M.S. Brown, R.E. Hammer, J.L. Goldstein, and H. Shimano. 1998. Activation of cholesterol synthesis in preference to fatty acid synthesis in liver and adipose tissue of transgenic mice overproducing sterol regulatory element-binding protein-2. *J. Clin. Invest.* 101:2331–2339. https://doi.org/10.1172/JCI2961

Hozoji-Inada, M., Y. Munehira, K. Nagao, N. Kioka, and K. Ueda. 2011. Liver X receptor beta (LXRbeta) interacts directly with ATP-binding cassette A1 (ABCA1) to promote high density lipoprotein formation during acute cholesterol accumulation. *J. Biol. Chem.* 286:20117–20124. https://doi.org/10.1074/jbc.M111.235846

Humpton, T.J., B. Alagesan, G.M. DeNicola, D. Lu, G.N. Yordanov, C.S. Leonhardt, M.A. Yao, P. Alagesan, M.N. Zaatari, Y. Park, et al. 2019. Oncogenic KRAS Induces NIX-Mediated Mitophagy to Promote Pancreatic Cancer. *Cancer Discov.* 9:1268–1287. https://doi.org/10.1158/2159-8290.CD-18-1409

Ikonen, E.. 2008. Cellular cholesterol trafficking and compartmentalization. *Nat. Rev. Mol. Cell Biol.* 9:125–138. https://doi.org/10.1038/nrm2336

Jiang, Y., A. Sun, Y. Zhao, W. Ying, H. Sun, X. Yang, B. Xing, W. Sun, L. Ren, B. Hu, et al; Chinese Human Proteome Project (CNHPP) Consortium. 2019. Proteomics identifies new therapeutic targets of early-stage hepatocellular carcinoma. *Nature.* 567:257–261. https://doi.org/10.1038/s41586-019-0987-8

Karasinska, J.M., J.T. Topham, S.E. Kalloger, G.H. Jang, R.E. Denroche, L. Culibrk, L.M. Williamson, H.L. Wong, M.K.C. Lee, G.M. O'Kane, et al. 2020. Altered Gene Expression along the Glycolysis-Cholesterol Synthesis Axis Is Associated with Outcome in Pancreatic Cancer. *Clin. Cancer Res.* 26:135–146. https://doi.org/10.1158/1078-0432.CCR-19-1543

Kaymak, I., C.R. Maier, W. Schmitz, A.D. Campbell, B. Dankworth, C.P. Ade, S. Walz, M. Paauwe, C. Kalogirou, H. Marouf, et al. 2020. Mevalonate pathway provides ubiquinone to maintain pyrimidine synthesis and survival in p53-deficient cancer cells exposed to metabolic stress. *Cancer Res.* 80:189–203. https://doi.org/10.1158/0008-5472.CAN-19-0650

Kendall, J., and A. Krasnitz. 2014. Computational methods for DNA copy-number analysis of tumors. *Methods Mol. Biol.* 1176:243–259. https://doi.org/10.1007/978-1-4939-0992-6_20

Kent, W.J., C.W. Sugnet, T.S. Furey, K.M. Roskin, T.H. Pringle, A.M. Zahler, and D. Haussler. 2002. The human genome browser at UCSC. *Genome Res.* 12:996–1006. https://doi.org/10.1101/gr.229102

Komor, A.C., Y.B. Kim, M.S. Packer, J.A. Zuris, and D.R. Liu. 2016. Programmable editing of a target base in genomic DNA without double-stranded DNA cleavage. *Nature.* 533:420–424. https://doi.org/10.1038/nature17946

Kusama, T., M. Mukai, T. Iwasaki, M. Tatsuta, Y. Matsumoto, H. Akedo, M. Inoue, and H. Nakamura. 2002. 3-hydroxy-3-methylglutaryl-coenzyme a reductase inhibitors reduce human pancreatic cancer cell invasion and metastasis. *Gastroenterology.* 122:308–317. https://doi.org/10.1053/gast.2002.31093

Langmead, B., and S.L. Salzberg. 2012. Fast gapped-read alignment with Bowtie 2. *Nat. Methods.* 9:357–359. https://doi.org/10.1038/nmeth.1923

Larsson, O.. 1996. HMG-CoA reductase inhibitors: role in normal and malignant cells. *Crit. Rev. Oncol. Hematol.* 22:197–212. https://doi.org/10.1016/1040-8428(96)00193-X

Leek, J.T., W.E. Johnson, H.S. Parker, A.E. Jaffe, and J.D. Storey. 2012. The sva package for removing batch effects and other unwanted variation in high-throughput experiments. *Bioinformatics.* 28:882–883. https://doi.org/10.1093/bioinformatics/bts034

Li, B., and C.N. Dewey. 2011. RSEM: accurate transcript quantification from RNA-Seq data with or without a reference genome. *BMC Bioinformatics.* 12:323. https://doi.org/10.1186/1471-2105-12-323

Li, J., D. Gu, S.S. Lee, B. Song, S. Bandyopadhyay, S. Chen, S.F. Konieczny, T.L. Ratliff, X. Liu, J. Xie, et al. 2016. Abrogating cholesterol esterification suppresses growth and metastasis of pancreatic cancer. *Oncogene.* 35:6378–6388. https://doi.org/10.1038/onc.2016.168

Liao, J., Y.T. Chung, A.L. Yang, M. Zhang, H. Li, W. Zhang, L. Yan, and G.Y. Yang. 2013. Atorvastatin inhibits pancreatic carcinogenesis and increases survival in LSL-KrasG12D-LSL-Trp53R172H-Pdx1-Cre mice. *Mol. Carcinog.* 52:739–750. https://doi.org/10.1002/mc.21916

Longo, J., P.J. Mullen, R. Yu, J.E. van Leeuwen, M. Masoomian, D.T.S. Woon, Y. Wang, E.X. Chen, R.J. Hamilton, J.M. Sweet, et al. 2019. An actionable sterol-regulated feedback loop modulates statin sensitivity in prostate cancer. *Mol. Metab.* 25:119–130. https://doi.org/10.1016/j.molmet.2019.04.003

Love, M.I., W. Huber, and S. Anders. 2014. Moderated estimation of fold change and dispersion for RNA-seq data with DESeq2. *Genome Biol.* 15:550. https://doi.org/10.1186/s13059-014-0550-8

Lüttges, J., H. Galehdari, V. Bröcker, I. Schwarte-Waldhoff, D. Henne-Bruns, G. Klöppel, W. Schmiegel, and S.A. Hahn. 2001. Allelic loss is often the first hit in the biallelic inactivation of the p53 and DPC4 genes during pancreatic carcinogenesis. *Am. J. Pathol.* 158:1677–1683. https://doi.org/10.1016/S0002-9440(10)64123-5

Marino, S., M. Vooijs, H. van Der Gulden, J. Jonkers, and A. Berns. 2000. Induction of medulloblastomas in p53-null mutant mice by somatic inactivation of Rb in the external granular layer cells of the cerebellum. *Genes Dev.* 14:994–1004.

Maxfield, F.R., and I. Tabas. 2005. Role of cholesterol and lipid organization in disease. *Nature.* 438:612–621. https://doi.org/10.1038/nature04399

Meiner, V.L., S. Cases, H.M. Myers, E.R. Sande, S. Bellosta, M. Schambelan, R.E. Pitas, J. McGuire, J. Herz, and R.V. Farese, Jr.. 1996. Disruption of the acyl-CoA:cholesterol acyltransferase gene in mice: evidence suggesting multiple cholesterol esterification enzymes in mammals. *Proc. Natl. Acad. Sci. USA*. 93:14041–14046. https://doi.org/10.1073/pnas.93.24.14041

Mo, H., R. Jeter, A. Bachmann, S.T. Yount, C.L. Shen, and H. Yeganehjoo. 2019. The Potential of Isoprenoids in Adjuvant Cancer Therapy to Reduce Adverse Effects of Statins. *Front. Pharmacol*. 9:1515. https://doi.org/10.3389/fphar.2018.01515

Moon, S.H., C.H. Huang, S.L. Houlihan, K. Regunath, W.A. Freed-Pastor, J.P. Morris, IV, D.F. Tschaharganeh, E.R. Kastenhuber, A.M. Barsotti, R. Culp-Hill, et al. 2019. p53 Represses the Mevalonate Pathway to Mediate Tumor Suppression. *Cell*. 176:564–580.e19. https://doi.org/10.1016/j.cell.2018.11.011

Ness, G.C., C.M. Chambers, and D. Lopez. 1998. Atorvastatin action involves diminished recovery of hepatic HMG-CoA reductase activity. *J. Lipid Res*. 39:75–84.

Oelkers, P., A. Behari, D. Cromley, J.T. Billheimer, and S.L. Sturley. 1998. Characterization of two human genes encoding acyl coenzyme A:cholesterol acyltransferase-related enzymes. *J. Biol. Chem*. 273:26765–26771. https://doi.org/10.1074/jbc.273.41.26765

Olive, K.P., D.A. Tuveson, Z.C. Ruhe, B. Yin, N.A. Willis, R.T. Bronson, D. Crowley, and T. Jacks. 2004. Mutant p53 gain of function in two mouse models of Li-Fraumeni syndrome. *Cell*. 119:847–860. https://doi.org/10.1016/j.cell.2004.11.004

Oram, J.F., and A.M. Vaughan. 2000. ABCA1-mediated transport of cellular cholesterol and phospholipids to HDL apolipoproteins. *Curr. Opin. Lipidol*. 11:253–260. https://doi.org/10.1097/00041433-200006000-00005

Philips, M.R.. 2012. Ras hitchhikes on PDE6δ. *Nat. Cell Biol*. 14:128–129. https://doi.org/10.1038/ncb2429

Premsrirut, P.K., L.E. Dow, S.Y. Kim, M. Camiolo, C.D. Malone, C. Miething, C. Scuoppo, J. Zuber, R.A. Dickins, S.C. Kogan, et al. 2011. A rapid and scalable system for studying gene function in mice using conditional RNA interference. *Cell*. 145:145–158. https://doi.org/10.1016/j.cell.2011.03.012

Radhakrishnan, A., J.L. Goldstein, J.G. McDonald, and M.S. Brown. 2008. Switch-like control of SREBP-2 transport triggered by small changes in ER cholesterol: a delicate balance. *Cell Metab*. 8:512–521. https://doi.org/10.1016/j.cmet.2008.10.008

Ridley, A.J.. 2013. RhoA, RhoB and RhoC have different roles in cancer cell migration. *J. Microsc*. 251:242–249. https://doi.org/10.1111/jmi.12025

Riscal, R., N. Skuli, and M.C. Simon. 2019. Even Cancer Cells Watch Their Cholesterol!. *Mol. Cell*. 76:220–231. https://doi.org/10.1016/j.molcel.2019.09.008

Roe, J.S., C.I. Hwang, T.D.D. Somerville, J.P. Milazzo, E.J. Lee, B. Da Silva, L. Maiorino, H. Tiriac, C.M. Young, K. Miyabayashi, et al. 2017. Enhancer Reprogramming Promotes Pancreatic Cancer Metastasis. *Cell*. 170:875–888.e20. https://doi.org/10.1016/j.cell.2017.07.007

Ruscetti, M., J. Leibold, M.J. Bott, M. Fennell, A. Kulick, N.R. Salgado, C.C. Chen, Y.J. Ho, F.J. Sanchez-Rivera, J. Feucht, et al. 2018. NK cell-mediated cytotoxicity contributes to tumor control by a cytostatic drug combination. *Science*. 362:1416–1422. https://doi.org/10.1126/science.aas9090

Sato, R., J. Inoue, Y. Kawabe, T. Kodama, T. Takano, and M. Maeda. 1996. Sterol-dependent transcriptional regulation of sterol regulatory element-binding protein-2. *J. Biol. Chem*. 271:26461–26464. https://doi.org/10.1074/jbc.271.43.26461

Siegel, R.L., K.D. Miller, and A. Jemal. 2019. Cancer statistics, 2019. *CA Cancer J. Clin*. 69:7–34. https://doi.org/10.3322/caac.21551

Sorrentino, G., N. Ruggeri, V. Specchia, M. Cordenonsi, M. Mano, S. Dupont, A. Manfrin, E. Ingallina, R. Sommaggio, S. Piazza, et al. 2014. Metabolic control of YAP and TAZ by the mevalonate pathway. *Nat. Cell Biol*. 16:357–366. https://doi.org/10.1038/ncb2936

Sousa, C.M., D.E. Biancur, X. Wang, C.J. Halbrook, M.H. Sherman, L. Zhang, D. Kremer, R.F. Hwang, A.K. Witkiewicz, H. Ying, et al. 2016. Pancreatic stellate cells support tumour metabolism through autophagic alanine secretion. *Nature*. 536:479–483. https://doi.org/10.1038/nature19084

Stechman, M.J., B.N. Ahmad, N.Y. Loh, A.A. Reed, M. Stewart, S. Wells, T. Hough, L. Bentley, R.D. Cox, S.D. Brown, et al. 2010. Establishing normal plasma and 24-hour urinary biochemistry ranges in C3H, BALB/c and C57BL/6J mice following acclimatization in metabolic cages. *Lab. Anim*. 44:218–225. https://doi.org/10.1258/la.2010.009128

Tang, Z., C. Li, B. Kang, G. Gao, C. Li, and Z. Zhang. 2017. GEPIA: a web server for cancer and normal gene expression profiling and interactive analyses. *Nucleic Acids Res*. 45(W1):W98–W102. https://doi.org/10.1093/nar/gkx247

Tiriac, H., P. Belleau, D.D. Engle, D. Plenker, A. Deschênes, T.D.D. Somerville, F.E.M. Froeling, R.A. Burkhart, R.E. Denroche, G.H. Jang, et al. 2018. Organoid Profiling Identifies Common Responders to Chemotherapy in Pancreatic Cancer. *Cancer Discov*. 8:1112–1129. https://doi.org/10.1158/2159-8290.CD-18-0349

Turrell, F.K., E.M. Kerr, M. Gao, H. Thorpe, G.J. Doherty, J. Cridge, D. Shorthouse, A. Speed, S. Samarajiwa, B.A. Hall, et al. 2017. Lung tumors with distinct p53 mutations respond similarly to p53 targeted therapy but exhibit genotype-specific statin sensitivity. *Genes Dev*. 31:1339–1353. https://doi.org/10.1101/gad.298463.117

Vassilev, L.T., B.T. Vu, B. Graves, D. Carvajal, F. Podlaski, Z. Filipovic, N. Kong, U. Kammlott, C. Lukacs, C. Klein, et al. 2004. In vivo activation of the p53 pathway by small-molecule antagonists of MDM2. *Science*. 303:844–848. https://doi.org/10.1126/science.1092472

Volkmar, N., M.L. Thezenas, S.M. Louie, S. Juszkiewicz, D.K. Nomura, R.S. Hegde, B.M. Kessler, and J.C. Christianson. 2019. The ER membrane protein complex promotes biogenesis of sterol-related enzymes maintaining cholesterol homeostasis. *J. Cell Sci*. 132. jcs223453. https://doi.org/10.1242/jcs.223453

Waller, D.D., J. Park, and Y.S. Tsantrizos. 2019. Inhibition of farnesyl pyrophosphate (FPP) and/or geranylgeranyl pyrophosphate (GGPP) biosynthesis and its implication in the treatment of cancers. *Crit. Rev. Biochem. Mol. Biol*. 54:41–60. https://doi.org/10.1080/10409238.2019.1568964

Whyte, D.B., P. Kirschmeier, T.N. Hockenberry, I. Nunez-Oliva, L. James, J.J. Catino, W.R. Bishop, and J.K. Pai. 1997. K- and N-Ras are geranylgeranylated in cells treated with farnesyl protein transferase inhibitors. *J. Biol. Chem*. 272:14459–14464. https://doi.org/10.1074/jbc.272.22.14459

Widenmaier, S.B., N.A. Snyder, T.B. Nguyen, A. Arduini, G.Y. Lee, A.P. Arruda, J. Saksi, A. Bartelt, and G.S. Hotamisligil. 2017. NRF1 Is an ER Membrane Sensor that Is Central to Cholesterol Homeostasis. *Cell*. 171:1094–1109.e15. https://doi.org/10.1016/j.cell.2017.10.003

Ying, H., A.C. Kimmelman, C.A. Lyssiotis, S. Hua, G.C. Chu, E. Fletcher-Sananikone, J.W. Locasale, J. Son, H. Zhang, J.L. Coloff, et al. 2012. Oncogenic Kras maintains pancreatic tumors through regulation of anabolic glucose metabolism. *Cell*. 149:656–670. https://doi.org/10.1016/j.cell.2012.01.058

Yue, S., J. Li, S.Y. Lee, H.J. Lee, T. Shao, B. Song, L. Cheng, T.A. Masterson, X. Liu, T.L. Ratliff, et al. 2014. Cholesteryl ester accumulation induced by PTEN loss and PI3K/AKT activation underlies human prostate cancer aggressiveness. *Cell Metab*. 19:393–406. https://doi.org/10.1016/j.cmet.2014.01.019

Zhang, F.L., and P.J. Casey. 1996. Protein prenylation: molecular mechanisms and functional consequences. *Annu. Rev. Biochem*. 65:241–269. https://doi.org/10.1146/annurev.bi.65.070196.001325

Zhang, Y., M. Liang, C. Sun, G. Qu, T. Shi, M. Min, Y. Wu, and Y. Sun. 2019. Statin Use and Risk of Pancreatic Cancer: An Updated Meta-analysis of 26 Studies. *Pancreas*. 48:142–150. https://doi.org/10.1097/MPA.0000000000001226

Zhao, Z., C.C. Chen, C.D. Rillahan, R. Shen, T. Kitzing, M.E. McNerney, E. Diaz-Flores, J. Zuber, K. Shannon, M.M. Le Beau, et al. 2015. Cooperative loss of RAS feedback regulation drives myeloid leukemogenesis. *Nat. Genet*. 47:539–543. https://doi.org/10.1038/ng.3251

Supplemental material

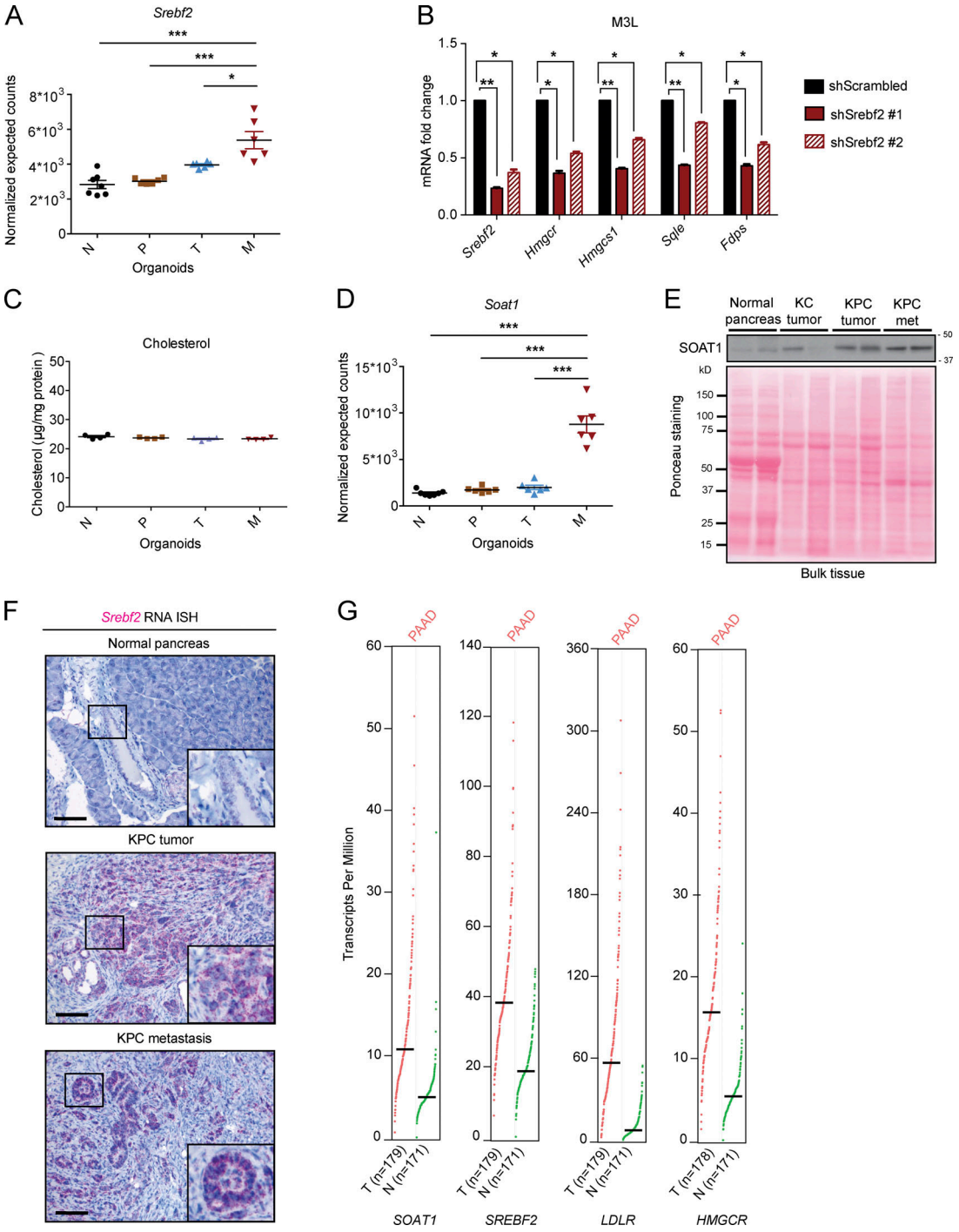

Figure S1. **SOAT1 expression increases during PDAC progression. (A)** RNA-seq analysis of *Srebf2* in murine N (n = 7), P (n = 6), T (n = 6), and tumor-matched M (n = 6) pancreatic organoids. Results show mean ± SEM. *, P < 0.05; ***, P < 0.001, paired Student's t test between matched T and M organoids; unpaired Student's t test between N, P, and M organoids. **(B)** qPCR analysis of *Srebf2*, *Hmgcr*, *Hmgcs1*, *Sqle*, and *Fdps* in M3L organoids with or without expression of two different shRNAs targeting *Srebf2*. Results show mean ± SD of two technical replicates. *, P < 0.05; **, P < 0.01, paired Student's t test. **(C)** Cholesterol assays for N (n = 4), P (n = 4), T (n = 4), and tumor-matched M (n = 4) organoids. Results show mean ± SEM of two biological replicates (two technical replicates each). No statistical difference was found, as calculated by paired Student's t test. **(D)** RNA-seq analysis of *Soat1* in N (n = 7), P (n = 6), T (n = 6), and tumor-matched M (n = 6) organoids. Results show mean ± SEM. ***, P < 0.001, paired Student's t test between matched T and M organoids; unpaired Student's t test between N, P, and M organoids. **(E)** Western blot analysis of SOAT1 (n = 2) in C57BL/6J normal pancreata (n = 2), KC tumors (n = 2), KPC tumors (n = 2), and KPC metastases (n = 2). Ponceau staining, loading control. Molecular weights in kilodaltons. **(F)** Representative RNA ISH for *Srebf2* in C57BL/6J normal pancreas (n = 3), KPC tumor (n = 3), and matched metastasis (n = 3). Inserts: magnification. Scale bars, 200 µm. **(G)** RNA expression analysis of *SOAT1*, *SREBF2*, *LDLR*, and *HMGCR* in human PDAC (T, n = 179) and normal pancreas (N, n = 171) from the GEPIA tool.

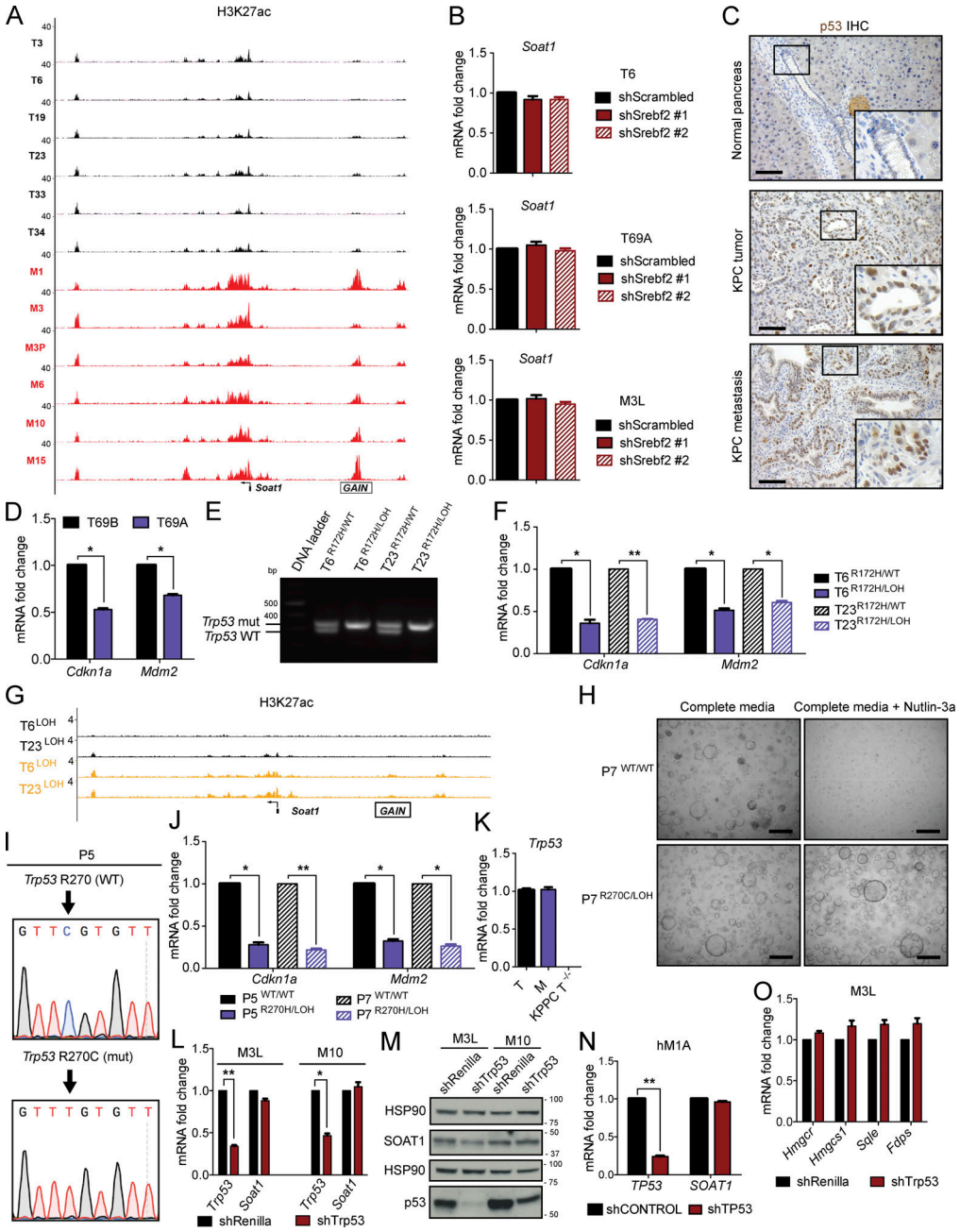

Figure S2. **SOAT1 expression is dependent on p53 status. (A)** Representative H3K27ac ChIP-seq profiles at the *Soat1* locus in matched T (n = 6) and M (n = 6) organoids. **(B)** qPCR analyses of *Soat1* in T6, T69A, and M3L organoids with or without expression of two different shRNAs targeting *Srebf2*. Results show mean ± SD of two technical replicates. No statistical difference was found, as calculated by paired Student's t test. **(C)** Representative IHC of p53 in C57BL/6J normal pancreas (n = 3), KPC tumor (n = 3), and metastasis (n = 3). Inserts: magnification. Scale bars, 200 µm. **(D)** qPCR analysis of *Cdkn1a* and *Mdm2* in T69B and T69A organoids. Results show mean ± SD of two technical replicates. *, P < 0.05, paired Student's t test. **(E)** DNA gel showing *Trp53* genetic status in T6 and T23 organoids with or without p53 LOH. mut, mutant. **(F)** qPCR analysis of *Cdkn1a* and *Mdm2* in T6 and T23 organoids with or without p53 LOH. Results show mean ± SD of two technical replicates. *, P < 0.05; **, P < 0.01, paired Student's t test. **(G)** Representative H3K27ac ChIP-seq profiles at the *Soat1* locus in T6 and T23 organoids with or without p53 LOH. **(H)** Representative bright-field images of P7 with $p53^{WT/WT}$ or $p53^{R270C/LOH}$ in complete media or complete media containing 10 µM Nutlin-3a. Scale bars, 800 µm. **(I)** DNA sequencing results showing *Trp53* mutation following base-editing in P5 P organoids. **(J)** qPCR analysis of *Cdkn1a* and *Mdm2* in P5 and P7 organoids with $p53^{WT/WT}$ or $p53^{R270C/LOH}$. Results show mean ± SD of two technical replicates. *, P < 0.05; **, P < 0.01, paired Student's t test. **(K)** qPCR analysis of *Trp53* in T (T3a, T6, and T23), M (M1, M3L, and M10), and KPPC $T^{-/-}$ (T91, T113, and T118) organoids. Results show mean ± SD of three biological replicates. No *Trp53* transcript was detected in the three $T^{-/-}$ organoid lines. **(L)** qPCR analysis of *Trp53* and *Soat1* in M3L and M10 organoids with or without expression of an shRNA targeting *Trp53*. Results show mean ± SD of two technical replicates. *, P < 0.05; **, P < 0.01, paired Student's t test. **(M)** Western blot analysis of p53 and SOAT1 in M3L and M10 organoids with or without expression of an shRNA targeting *Trp53* (n = 2). HSP90, loading controls. Molecular weights in kilodaltons. **(N)** qPCR analysis of *TP53* and *SOAT1* in hM1A organoids with or without expression of an shRNA targeting *TP53*. Results show mean ± SD of two technical replicates. **, P < 0.01, paired Student's t test. **(O)** qPCR analysis of *Hmgcr*, *Hmgcs1*, *Sqle*, and *Fdps* in M3L organoids with or without expression of an shRNA targeting *Trp53*. Results show mean ± SD of two technical replicates. No statistical difference was found, as calculated by paired Student's t test.

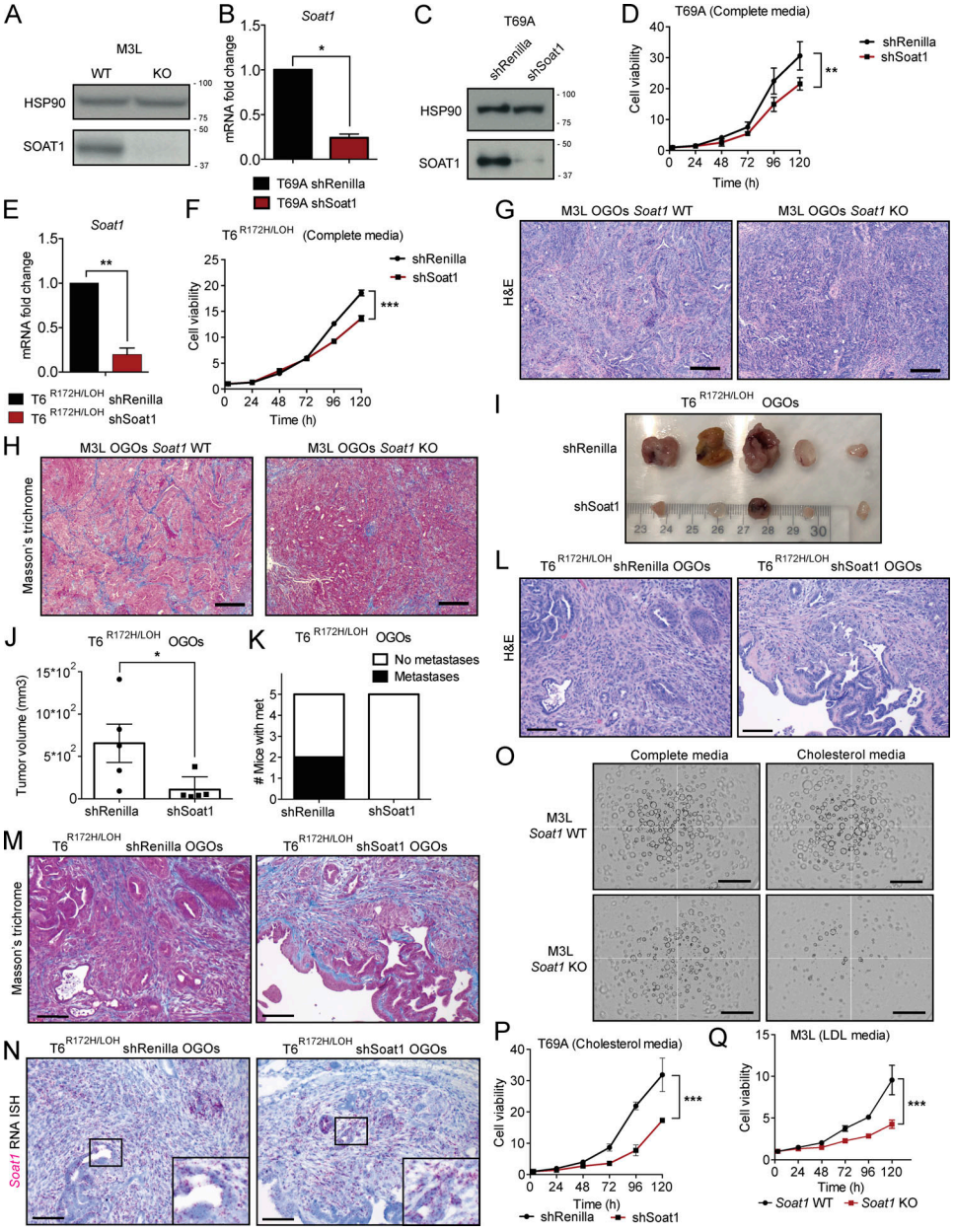

Figure S3. **SOAT1 loss significantly impairs PDAC progression. (A)** Western blot analysis of SOAT1 in M3L organoids with *Soat1* WT or KO (n = 2). HSP90, loading control. Molecular weights in kilodaltons. **(B)** qPCR analysis of *Soat1* in T69A organoids with or without expression of an shRNA targeting *Soat1*. Results show mean ± SD of two technical replicates. *, P < 0.05, paired Student's t test. **(C)** Western blot analysis of SOAT1 in T69A organoids with or without expression of an shRNA targeting *Soat1* (n = 2). HSP90, loading control. Molecular weights in kilodaltons. **(D)** Proliferation curves of T69A organoids with or without expression of an shRNA targeting *Soat1*. Results show mean ± SD of five technical replicates. **, P < 0.01, unpaired Student's t test calculated for the last time point. **(E)** qPCR analysis of *Soat1* in $T6^{R172H/LOH}$ organoids with or without expression of an shRNA targeting *Soat1*. Results show mean ± SD of three technical replicates. **, P < 0.01, paired Student's t test. **(F)** Proliferation curves of $T6^{R172H/LOH}$ organoids with or without expression of an shRNA targeting *Soat1*. Results show mean ± SD of five technical replicates. ***, P < 0.001, unpaired Student's t test calculated for the last time point. **(G)** Representative H&E stain of M3L OGO models with *Soat1* WT or KO (n = 3). Scale bars, 400 µm. **(H)** Representative Masson's trichrome stain of M3L OGO models with *Soat1* WT or KO (n = 3). Scale bars, 400 µm. **(I)** Images of $T6^{R172H/LOH}$ OGO models with or without expression of an shRNA targeting *Soat1* in *nu/nu* mice at day 24 after transplantation (n = 5 per cohort). **(J)** Quantification of tumor volumes of $T6^{R172H/LOH}$ OGO models shown in I. Results show mean ± SEM of five biological replicates per cohort. *, P < 0.05, unpaired Student's t test. **(K)** Number of mice with metastases for the experiment shown in I. **(L)** Representative H&E stain of $T6^{R172H/LOH}$ OGO models with or without expression of an shRNA targeting *Soat1* (n = 3). Scale bars, 200 µm. **(M)** Representative Masson's trichrome stain of $T6^{R172H/LOH}$ OGO models with or without expression of an shRNA targeting *Soat1* (n = 3). Scale bars, 200 µm. **(N)** Representative RNA ISH of *Soat1* in $T6^{R172H/LOH}$ OGO models with or without expression of an shRNA targeting *Soat1* (n = 3). Inserts: magnification. Scale bars, 200 µm. **(O)** Representative bright-field images of M3L organoids with or without *Soat1* KO in complete media or complete media containing 50 µM cholesterol at 96 h (n = 2). Scale bars, 800 µm. **(P)** Proliferation curves of T69A organoids with or without expression of an shRNA targeting *Soat1* in complete media containing 50 µM cholesterol. Results show mean ± SD of five technical replicates. ***, P < 0.001, unpaired Student's t test calculated for the last time point. **(Q)** Proliferation curves of M3L organoids with or without *Soat1* KO in complete media containing 0.5% LDL. Results show mean ± SD of five technical replicates. ***, P < 0.001, unpaired Student's t test calculated for the last time point.

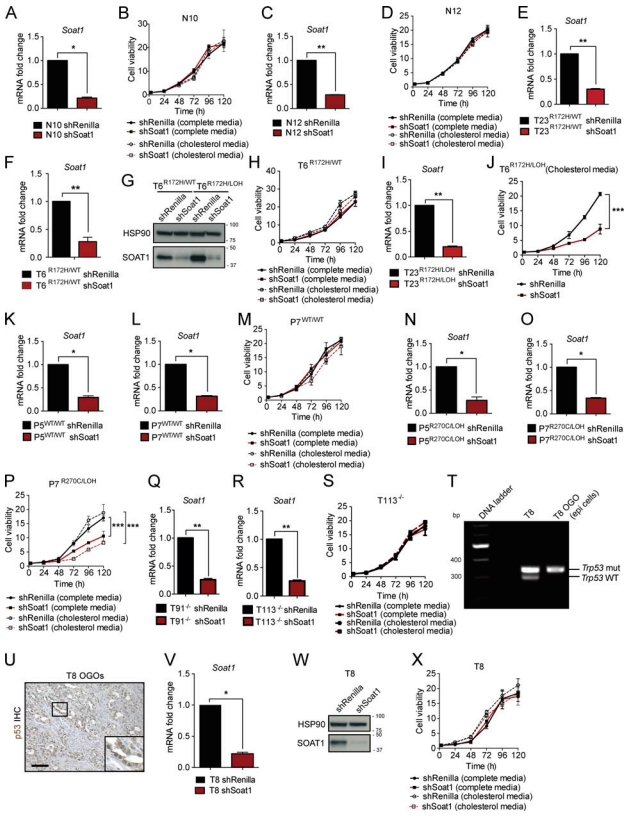

Figure S4. **p53 LOH sensitizes tumor cells to SOAT1 deficiency. (A)** qPCR analysis of *Soat1* in N10 N organoids with or without expression of an shRNA targeting *Soat1*. Results show mean ± SD of two technical replicates. *, P < 0.05, paired Student's *t* test. **(B)** Proliferation curves of N10 organoids with or without expression of an shRNA targeting *Soat1* in complete media or complete media containing 50 µM cholesterol. Results show mean ± SD of five technical replicates. No statistical difference was found, as calculated by unpaired Student's *t* test for the last time point. **(C)** qPCR analysis of *Soat1* in normal N12 organoids with or without expression of an shRNA targeting *Soat1*. Results show mean ± SD of two technical replicates. **, P < 0.01, paired Student's *t* test. **(D)** Proliferation curves of N12 organoids with or without expression of an shRNA targeting *Soat1* in complete media or complete media containing 50 µM cholesterol. Results show mean ± SD of five technical replicates. No statistical difference was found, as calculated by unpaired Student's *t* test for the last time point. **(E)** qPCR analysis of *Soat1* in $T23^{R172H/WT}$ organoids with or without expression of an shRNA targeting *Soat1*. Results show mean ± SD of two technical replicates. **, P < 0.01, paired Student's *t* test. **(F)** qPCR analysis of *Soat1* in $T6^{R172H/WT}$ organoids with or without expression of an shRNA targeting *Soat1*. Results show mean ± SD of three technical replicates. **, P < 0.01, paired Student's *t* test. **(G)** Western blot analysis of SOAT1 in $T6^{R172H//WT}$ and $T6^{R172H/LOH}$ organoids with or without expression of an shRNA targeting *Soat1* (*n* = 2). HSP90, loading control. Molecular weights in kilodaltons. **(H)** Proliferation curves of $T6^{R172H/WT}$ organoids with or without expression of an shRNA targeting *Soat1* in complete media or complete media containing 50 µM cholesterol. Results show mean ± SD of five technical replicates. No statistical difference was found, as calculated by unpaired Student's *t* test for the last time point. **(I)** qPCR analysis of *Soat1* in $T23^{R172H/LOH}$ organoids with or without expression of an shRNA targeting *Soat1*. Results show mean ± SD of two technical replicates. **, P < 0.01, paired Student's *t* test. **(J)** Proliferation curves of $T6^{R172H/LOH}$ organoids with or without expression of an shRNA targeting *Soat1* in complete media containing 50 µM cholesterol. Results show mean ± SD of five technical replicates. ***, P < 0.001, unpaired Student's *t* test calculated for the last time point. **(K)** qPCR analysis of *Soat1* in P5 P organoids with $p53^{WT/WT}$ with or without expression of an shRNA targeting *Soat1*. Results show mean ± SD of two technical replicates. *, P < 0.05, paired Student's *t* test. **(L)** qPCR analysis of *Soat1* in P7 organoids with $p53^{WT/WT}$ with or without expression of an shRNA targeting *Soat1*. Results show mean ± SD of two technical replicates. *, P < 0.05, paired Student's *t* test. **(M)** Proliferation curves of P7 organoids with $p53^{WT/WT}$ with or without expression of an shRNA targeting *Soat1* in complete media or complete media containing 50 µM cholesterol. Results show mean ± SD of five technical replicates. No statistical difference was found, as calculated by unpaired Student's *t* test for the last time point. **(N)** qPCR analysis of *Soat1* in P5 organoids with $p53^{R270C/LOH}$ with or without expression of an shRNA targeting *Soat1*. Results show mean ± SD of two technical replicates. *, P < 0.05, paired Student's *t* test. **(O)** qPCR analysis of *Soat1* in P7 organoids with $p53^{R270C/LOH}$ with or without expression of an shRNA targeting *Soat1*. Results show mean ± SD of two technical replicates. *, P < 0.05, paired Student's *t* test. **(P)** Proliferation curves of P7 organoids with $p53^{R270C/LOH}$ with or without expression of an shRNA targeting *Soat1* in complete media or complete media containing 50 µM cholesterol. Results show mean ± SD of five technical replicates. ***, P < 0.001, unpaired Student's *t* test calculated for the last time point. **(Q)** qPCR analysis of *Soat1* in $T91^{-/-}$ organoids with or without expression of an shRNA targeting *Soat1*. Results show mean ± SD of two technical replicates. **, P < 0.01, paired Student's *t* test. **(R)** qPCR analysis of *Soat1* in $T113^{-/-}$ organoids with or without expression of an shRNA targeting *Soat1*. Results show mean ± SD of two technical replicates. **, P < 0.01, paired Student's *t* test. **(S)** Proliferation curves of $T113^{-/-}$ organoids with or without expression of an shRNA targeting *Soat1* in complete media or complete media containing 50 µM cholesterol. Results show mean ± SD of five technical replicates. No statistical difference was found, as calculated by unpaired Student's *t* test for the last time point. **(T)** DNA gel showing *Trp53* genetic status in T8 organoids and in $DAPI^{-}$ $CD45^{-}$ $CD31^{-}$ $PDPN^{-}$ $EpCAM^{+}$ epithelial cancer cells sorted from T8 OGO models. mut, mutant. **(U)** Representative IHC of p53 in T8 OGO models (*n* = 2). Insert: magnification. Scale bar, 200 µm. **(V)** qPCR analysis of *Soat1* in T8 organoids with or without expression of an shRNA targeting *Soat1*. Results show mean ± SD of two technical replicates. *, P < 0.05, paired Student's *t* test. **(W)** Western blot analysis of SOAT1 in T8 organoids with or without expression of an shRNA targeting *Soat1* (*n* = 2). HSP90, loading control. Molecular weights in kilodaltons. **(X)** Proliferation curves of T8 organoids with or without expression of an shRNA targeting *Soat1* in complete media or complete media containing 50 µM cholesterol. Results show mean ± SD of five technical replicates. No statistical difference was found, as calculated by unpaired Student's *t* test for the last time point.

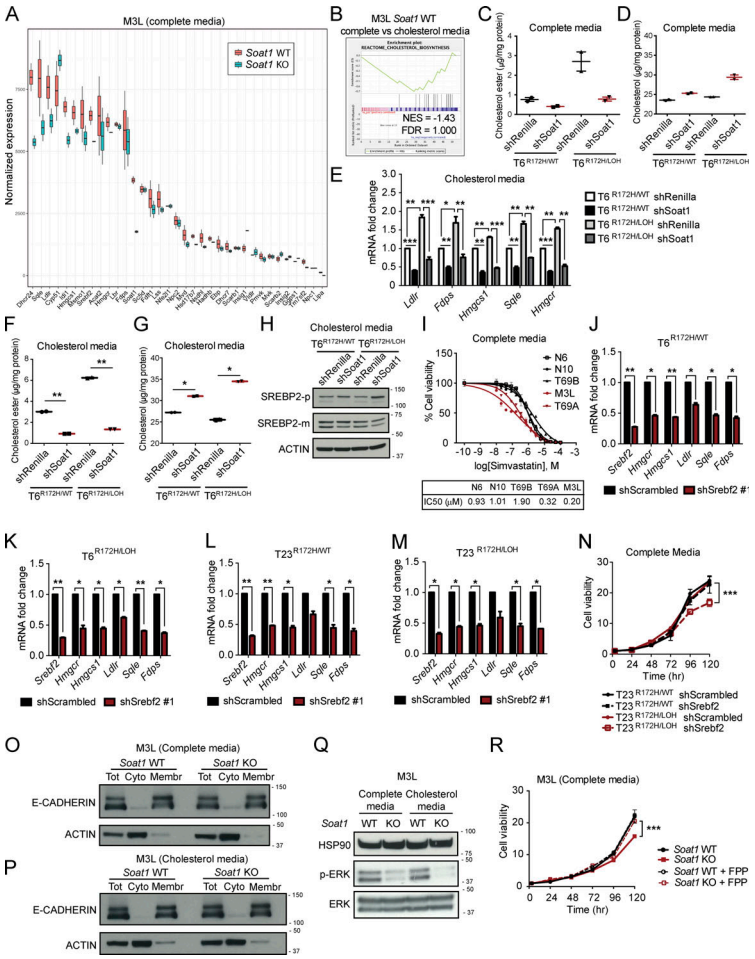

Figure S5. **SOAT1 expression sustains the mevalonate pathway in PDAC. (A)** Box plots of RNA-seq expression in M3L organoids with *Soat1* WT (n = 2) or KO (n = 2) in complete media for 24 h showing genes involved in cholesterol metabolism. Box sizes reflects expression ranges ± SD between two technical replicates. **(B)** GSEA plot for cholesterol biosynthesis in M3L organoids with *Soat1* WT in complete media or complete media containing 50 µM cholesterol for 24 h. NES, normalized enrichment score. No statistical difference was found based on NES and FDR. **(C)** Cholesterol ester assays for $T6^{R172H/WT}$ and $T6^{R172H/LOH}$ organoids with or without expression of an shRNA targeting *Soat1* in complete media for 4 h. Results show mean ± SD of two technical replicates. No statistical difference was found, as calculated by paired Student's *t* test. **(D)** Cholesterol assays for $T6^{R172H/WT}$ and $T6^{R172H/LOH}$ organoids with or without expression of an shRNA targeting *Soat1* in complete media for 4 h. Results show mean ± SD of two technical replicates. No statistical difference was found, as calculated by paired Student's *t* test. **(E)** qPCR analysis of *Ldlr*, *Fdps*, *Hmgcs1*, *Sqle*, and *Hmgcr* in $T6^{R172H/WT}$ and $T6^{R172H/LOH}$ organoids with or without expression of an shRNA targeting *Soat1* in complete media containing 50 µM cholesterol for 24 h. Results show mean ± SD of three technical replicates. *, P < 0.05; **, P < 0.01; ***, P < 0.001, paired Student's *t* test. **(F)** Cholesterol ester assays for $T6^{R172H/WT}$ and $T6^{R172H/LOH}$ organoids with or without expression of an shRNA targeting *Soat1* in complete media containing 50 µM cholesterol for 4 h. Results show mean ± SD of two technical replicates per cohort. **, P < 0.01, paired Student's *t* test. **(G)** Cholesterol assays for $T6^{R172H/WT}$ and $T6^{R172H/LOH}$ organoids with or without expression of an shRNA targeting *Soat1* in complete media containing 50 µM cholesterol for 4 h. Results show mean ± SD of two technical replicates per cohort. *, P < 0.05, paired Student's *t* test. **(H)** Western blot analysis of the inactive SREBP2 precursor (SREBP2-p) and mature SREBP2 protein (SREBP2-m) in $T6^{R172H/WT}$ and $T6^{R172H/LOH}$ organoids with or without expression of an shRNA targeting *Soat1* in complete media containing 50 µM cholesterol for 24 h (n = 2). ACTIN, loading control. **(I)** IC_{50} curves and values of N6, N10, T69B, T69A, and M3L organoids in complete media for 72 h with 1×10^{-10} M to 1×10^{-4} M Simvastatin. Results show mean ± SD of five technical replicates. **(J)** qPCR analysis of *Srebf2*, *Ldlr*, *Fdps*, *Hmgcs1*, *Sqle*, and *Hmgcr* in $T6^{R172H/WT}$ organoids with or without expression of an shRNA targeting *Srebf2* in complete media. Results show mean ± SD of two technical replicates. *, P < 0.05; **, P < 0.01, paired Student's *t* test. **(K)** qPCR analysis of *Srebf2*, *Ldlr*, *Fdps*, *Hmgcs1*, *Sqle*, and *Hmgcr* in $T6^{R172H/LOH}$ organoids with or without expression of an shRNA targeting *Srebf2* in complete media. Results show mean ± SD of two technical replicates. *, P < 0.05; **, P < 0.01, paired Student's *t* test. **(L)** qPCR analysis of *Srebf2*, *Ldlr*, *Fdps*, *Hmgcs1*, *Sqle*, and *Hmgcr* in $T23^{R172H/WT}$ organoids with or without expression of an shRNA targeting *Srebf2* in complete media. Results show mean ± SD of two technical replicates. *, P < 0.05; **, P < 0.01, paired Student's *t* test. **(M)** qPCR analysis of *Srebf2*, *Ldlr*, *Fdps*, *Hmgcs1*, *Sqle*, and *Hmgcr* in $T23^{R172H/LOH}$ organoids with or without expression of an shRNA targeting *Srebf2* in complete media. Results show mean ± SD of two technical replicates. *, P < 0.05, paired Student's *t* test. **(N)** Proliferation curves of $T23^{R172H/WT}$ and $T23^{R172H/LOH}$ organoids with or without expression of an shRNA targeting *Srebf2* in complete media. Results show mean ± SD of five technical replicates. ***, P < 0.001, unpaired Student's *t* test calculated for the last time point. **(O)** Western blot analysis of E-CADHERIN and ACTIN in total (Tot), cytoplasmic (Cyto) and membrane (Membr) protein fractions in M3L organoids with or without *Soat1* KO in complete media for 48 h. **(P)** Western blot analysis of E-CADHERIN and ACTIN in total (Tot), cytoplasmic (Cyto) and membrane (Membr) protein fractions in M3L organoids with or without *Soat1* KO in complete media containing 50 µM cholesterol for 48 h. **(Q)** Western blot analysis of phosphorylated ERK (p-ERK) and total ERK in M3L organoids with *Soat1* WT or KO in complete media or complete media containing 50 µM cholesterol for 48 h (n = 2). HSP90, loading control. **(R)** Proliferation curves of M3L organoids with *Soat1* WT or KO in complete media with or without 25 µM FPP. Results show mean ± SD of five technical replicates. ***, P < 0.001, unpaired Student's *t* test calculated for the last time point. Molecular weights in kilodaltons.

Tables S1 and S2 are provided online as separate Excel files. Table S1 contains the normalized expected counts for the RNA-seq analysis of murine pancreatic N, P, T, and M organoids shown in Fig. 1 and Fig. S1. Table S2 contains the DNA motif analysis performed using the *SREBF2* (MA0596.1) human motif.